CHALMERS

Aero Engine Intercooling

Conceptual design and experimental validation of an aero engine intercooler

XIN ZHAO

Department of Applied Mechanics
CHALMERS UNIVERSITY OF TECHNOLOGY
Gothenburg, Sweden 2016

THESIS FOR THE DEGREE OF DOCTOR OF PHILOSOPHY IN THERMO AND FLUID DYNAMICS

Aero Engine Intercooling

Conceptual design and experimental validation of an aero engine intercooler

XIN ZHAO

Department of Applied Mechanics
CHALMERS UNIVERSITY OF TECHNOLOGY
Gothenburg, Sweden 2016

Aero Engine Intercooling
Conceptual design and experimental validation of an aero engine intercooler
XIN ZHAO
ISBN 978-91-7597-380-7

Doktorsavhandlingar vid Chalmers tekniska högskola
Ny serie nr. 4061
ISSN 0346-718X
Department of Applied Mechanics
Chalmers University of Technology
SE-412 96 Gothenburg
Sweden
Telephone: +46 (0)31-772 1000

Chalmers Reproservice
Gothenburg, Sweden 2016

Aero Engine Intercooling
Conceptual design and experimental validation of an aero engine intercooler
Thesis for the degree of Doctor of Philosophy in Thermo and Fluid Dynamics
XIN ZHAO
Department of Applied Mechanics
Chalmers University of Technology

Abstract

Intercooling has the potential to provide a shortcut to the next generation aero engines with higher bypass ratio (BPR), higher overall pressure ratio (OPR) and higher turbine inlet temperature (TIT) by lowering the high pressure compressor (HPC) delivery temperature. To be able to establish a systematic understanding of aero engine intercooling, the heat transfer and pressure loss characteristics of a given intercooler architecture need to be known in the parameter range anticipated for the engine optimization. A two-pass cross flow tubular heat exchanger for aero engine intercooling applications was hence developed by the means of computational fluid dynamics (CFD). Optimizations with this intercooler installed were performed by considering the intercooler design parameters and the engine design simutaneously. A geared variant was adopted to complement the use of intercooling as it could support high OPR engines better by allowing a lower position installation of the HPC.

For a flight mission, further optimization of the intercooled engines was achieved by controlling the amount of intercooling for different engine operating points in two ways. One is intercooler external flow control by a separate variable nozzle and another one is intercooler internal flow variable flow path. As the flight altitude strongly influences the working condition for an aero engine, considerable SFC benefit can be obtained by limiting intercooling at high altitude operation. Nevertheless, the precondition is to enable a higher OPR at the take-off operation by intercooling.

Compared to a reference non-intercooled geared engine, an optimal intercooled geared engine with intercooling control shows a 4.9% better mission fuel burn under the same engine technology level assumptions. However, the optimum is still constrained by the last stage compressor blade height. To further explore the potential of intercooling the constraint limiting the axial compressor last stage blade height is relaxed by introducing an axial-radial combined HPC. The axial–radial high pressure ratio configuration allows for an ultrahigh OPR. With an optimal top-of-climb (TOC) OPR of 140, the configuration provides a 5.3% fuel burn benefit over the geared reference engine.

Experimental validation of the intercooler design and the CFD design tool is also presented in this thesis. With the help of particle image velocimetry (PIV) and pressure measurements, flow topology inside the intercooler was visualized. Generally, by comparing the CFD results and the experimental data, the computational capability of porous media modeling predicting the flow distribution within the tubular heat transfer units was confirmed. The flow topology within the associated ducts was considered well-described by CFD.

Keywords: intercooler, aero engine, CFD, system performance, porous media, intercooling control, variable flow path, PIV, pressure measurements

Never failed, Never lived. - I don't know who said this, but I like it.

Acknowledgements

Firstly, I would like to express my deep gratitude to my supervisor Professor Tomas Grönstedt for all the supports and trusts that he has given me over the years. It has been a pleasure to work with him, who has always shown enthusiastic attitude and great wit. I would also like to thank my co-supervisor Niklas Andersson for the discussions during the weekly meeting.

Anders Lundbladh from GKN Aerospace, and Andrew Rolt from Rolls-Royce UK, many thanks for sharing your knowledge and ideas with me. Also, Dennis Jacobsson from GKN Aerospace, thanks for the support in the LEMCOTEC project.

I am very grateful to Dr. Lei Xu from Siemens, Dr. Konstantinos Kyprianidis at Mälardalen University and Dr. Huadong Yao for their help and friendship.

I want to also express my acknowledgement to Erwin Adi Hartono, Mikhail Tokarev and associate professor Valery Chernoray for the help and support during the experiment.

Moreover, my special thanks to all in the Turbo Group and the Fluid Dynamics Division for the nice working atmosphere. Especially Ulla Lindberg-Thieme and Monica Vargman for their kind assistance.

Finally, my deepest gratitude to my family, my beloved wife Manlin Ye and my parents, for their support and confidence in me.

This work is financially supported by the E.U. under the 'LEMCOTEC - Low Emissions Core-Engine Technologies', a Collaborative Project co-funded by the European Commission within the Seventh Framework Programme (2007-2013) under the Grant Agreement 283216.

The experimental work is funded by the Swedish Energy Agency, Siemens Industrial Turbomachinery AB and GKN Aerospace through the Swedish research program TURBO POWER, the support of which is gratefully acknowledged.

The computer time at C3SE (Chalmers Center for Computational Science and Engineering) supported by SNIC (the Swedish National Infrastructure for Computing) is acknowledged.

Nomenclature

Abbreviations

BPR	Bypass ratio
CFD	Computational fluid dynamics
EIS	Entry into service
FPR	Fan pressure ratio
HPC	High pressure compressor
HPT	High pressure turbine
IPC	Intermediate pressure compressor
LEMCOTEC	Low emissions core technologies
LPT	Low pressure compressor
NEWAC	New aero engine core concepts
OPR	Overall pressure ratio
PIV	Particle image velocimetry
PR	Pressure ratio
RPK	Revenue passenger kilometers
SFC	Specific fuel consumption $[mg/N{\cdot}s]$
SST	Shear stress transport
TIT	Turbine inlet temperature [K]
TOC	Top-of-climb
TRL	Technology readiness level
VFP	Variable flow path
VSN	Variable separate nozzle

Latin symbols

A_c	Minimum flow cross section area of the computational domain $[m^2]$
A_f	Intercooler frontal area of the computational domain $[m^2]$
A_w	Heat transfer wall area of the computational domain $[m^2]$
a	Major axis length of the ellipse $[m]$
b	Minor axis length of the ellipse $[m]$
D	Hydraulic diameter of single elliptical tube $[m]$
D_h	Hydraulic diameter of a tube stack computational domain $[m]$
d_a	Axial spacing between tube columns $[m]$
d_b	Transversal spacing between tube rows $[m]$
f	Friction factor
h	Heat transfer coefficient $[J/(m^2{\cdot}s{\cdot}K)]$
j	Colburn j factor
k_{tube}	Tube internal flow loss coefficient
k'	Darcy pressure loss coefficient for porous media model
L	Total flow length of the intercooler $[m]$
$\dot{m}$	Mass flow rate $[kg/m^3]$
V	Flow Velocity $[m/s]$
Nu	Nusselt number
Pr	Prandtl number
Re	Reynolds number
St	Stanton number
Δp	Pressure drop $[Pa]$

Greek symbols

- ρ Density $[kg/m^3]$
- μ Dynamic Viscosity $[kg/(m \cdot s)]$
- η Efficiency
- κ Thermal conductivity of air $[J/(m \cdot s \cdot K)]$

Thesis

This thesis consists of an extended summary and the followed appended papers:

Paper A Zhao, X., Grönstedt, T. and Kyprianidis, K., **Assessment of The Performance Potential for a Two-pass Cross Flow Intercooler for Aero Engine Applications**. The 21st ISABE conference, September 9-13, 2013, Busan, South Korea.

Paper B Zhao, X. and Grönstedt, T., **Conceptual Design of a Two-Pass Cross Flow Aero-Engine Intercooler**. Proc IMechE Part G: Journal of Aerospace Engineering. 2014.

Paper C Zhao, X., Thulin, O., and Grönstedt, T., **First and Second Law Analysis of Intercooled Turbofan Engine**. ASME Journal of Engineering for Gas Turbines and Power. 2015.

Paper D Zhao, X. and Grönstedt, T., **Aero Engine Intercooling Optimization Using A Variable Flow Path**. The 22nd ISABE conference, October 25-30, 2015, Phoenix, USA.

Paper E Zhao, X. Tokarev, M, Hartono, A E., Chernoray, V., and Grönstedt, T., **Experimental Validation of The Aerodynamic Performance of An Aero Engine Intercooler**. Submitted for publication in a scientific journal.

Other related publications are listed here:

- Camilleri, W., Anselmi, E., Sethi, V., Laskaridis, P., Grönstedt, T., Zhao, X., Rolt, A., and Cobas, P., **Concept Description and Assessment of the Main Features of A Geared Intercooled Reversed Flow Core Engine**. Proc IMechE Part G: Journal of Aerospace Engineering. 2014.
- Petit, O., Xisto, C., Zhao, X. and Grönstedt, T., **An Outlook for Radical Aero Engine Intercooler Concepts**. Proceedings of ASME Turbo Expo 2016, GT2016-57920, June 13-16, Seoul, South Korea.

Contents

Part I
Extended Summary

This thesis focuses on establishing a systematic understanding of intercooling for aero engine applications, including the conceptual design and experimental validation of an intercooler system and the assessments of intercooled aero engines with the designed intercooler installed. It consists of an extended summary (Part I) and five appended papers (Part II). Below, an introduction of intercooling is given and the rationale of the study is established. Chapter 2 describes the conceptual design of the aero engine intercooler using mainly CFD. The established heat transfer and pressure loss characteristics of the intercooler are included. The assessments of intercooled aero engines with the designed intercooler are presented in Chapter 3. Chapter 4 gives the experimental validation of the design, mainly through the comparison between the measurements and the CFD results. Chapter 5 summarizes the associate papers to this thesis and Chapter 6 concludes the work presented in this thesis. Part II includes the appended papers.

1 Introduction

Since the time that the first heavier-than-air craft was successfully sent to the sky, the aviation industry has played an important role in the history of mankind. After the great progress of military jet propulsion, commercial air transportation enters an era of booming in the demand of economic development and globalization. In the most recent study reported by Airbus - Global Market Forecast 2015-2034 [1], air traffic will double in the next 15 years as shown in Figure 1.0.1 with an estimated 4.6% annual increase. This will lead to a demand for 32,600 new passenger and freighter aircraft by 2034. There is no doubt that it is a big cake for the aviation industry, however, it is not yet on the table. Accompanying the fruitful growth is an overloaded environment. Even though the global aviation industry now produces around only 2% of all human-induced carbon dioxide emissions, the continuous increase would lead to a dilemma for the aviation development. In early 2009, the aviation industry has set an ambitious target of halving the CO_2 emissions by 2050 compared to 2005. To achieve the target and keep a sustainable growth, the aviation industry must be able to provide long-term solutions of the technologies and operations. As the core part of an aircraft, the aero engine takes most of the pressure and challenge.

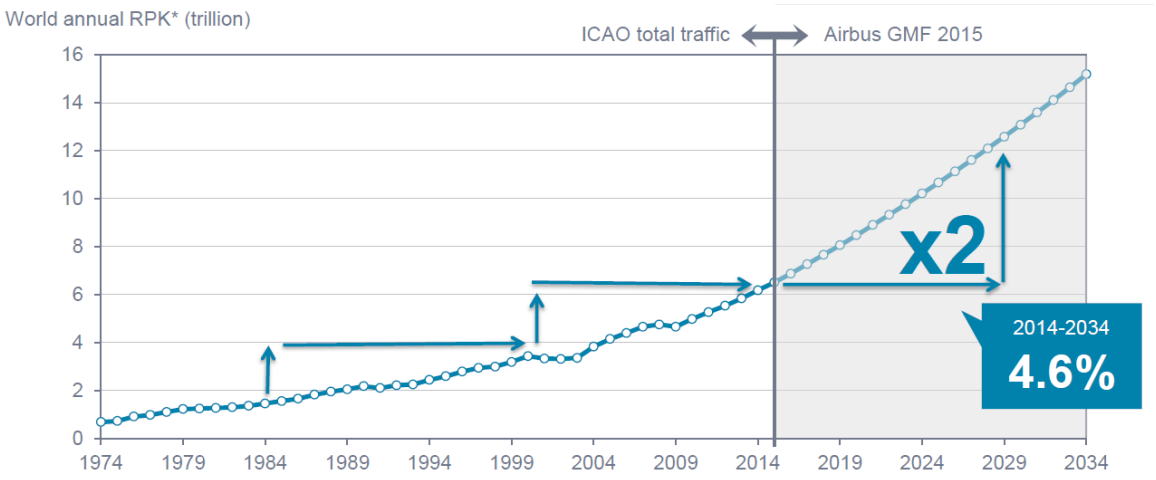

Figure 1.0.1: *World annual revenue passenger kilometers [1].*

1.1 Aero engine technology trend

After the first production turbofan Conway introduced by Rolls-Royce in 1950, every change in the development of aircraft engine is a revolution change of technology. As shown in Figure 1.1.1, from the old turbojet engine to turbofans with low BPRs and then to modern turbofans with high BPRs, higher BPR design giving lower fuel burn dominates the development of the engine technology. On the path of the future technology development, the improvement in the high BPR turbofan is slowing down and another revolution for a even higher BPR technology is needed in the following decades. Besides the BPR, the OPR and the TIT have been continuously pushed up as the general trends illustrated in Figure 1.1.2.

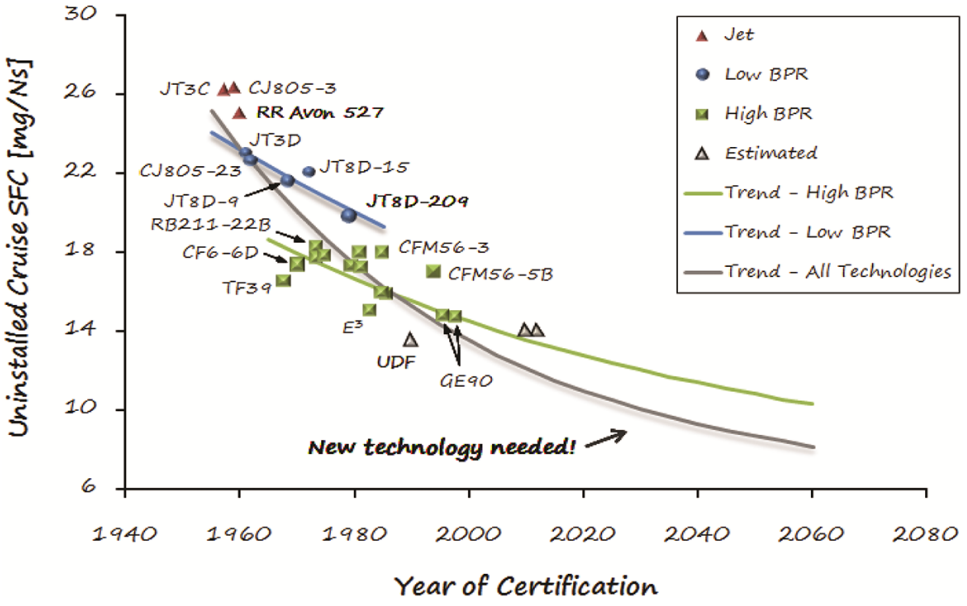

Figure 1.1.1: *Trends of jet engine technology development quantified in terms of uninstalled cruise SFC as a function of year of certification [2].*

At the present time, state-of-art large civil aero engines typically operate at BPR 10, OPR 40 and TIT 1800 K. Further increases in these parameters are however constrained. As the BPR increases, the fan size increases as well as the nacelle line and hence increases the induced nacelle drag. A larger fan size also increases the difficulty of designing an efficient fan. In addition, extra LPT stages may be required to drive the fan if the BPR is too high. For a larger OPR, the resulting higher cooling air temperature would increase the difficulty of turbine cooling and a higher TIT will further increase the requirement of turbine cooling and turbine material.

1.2 Intercooled cycle

In most thermodynamic and gas turbine textbooks, the intercooled cycle is introduced as a way to improve the specific work output of a gas turbine . As illustrated in Figure 1.2.1, the loop 1-2-3-4 represents the basic Brayton cycle while the loop 1-1a-1b-2'-3'-4' represents the intercooled cycle. By splitting the compression between a low pressure and a high pressure compressor and introducing an intercooler in between, the compression work required is reduced and a higher work output is obtained.

However, intercooling is actually a process of rejecting heat from the cycle. With a constant OPR and TIT, the intercooled cycle normally gives lower efficiency compared to the basic cycle. Considering the additional weight, size and losses introduced by the intercooler system, the intercooled cycle alone was not a popular selection for practical gas turbines in early years. More often, the intercooled cycle was considered in corporation with a regenerative cycle which could compensate the incurred thermal loss as shown in Figure 1.2.1b with 2a-2b-4a-4b. In the stationary and marine industry, the requirement on the size and weight of the powerplant is relatively

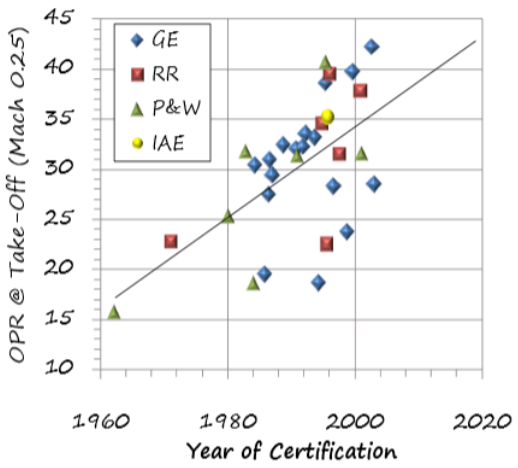

(a) *OPR as a function of engine certification year*

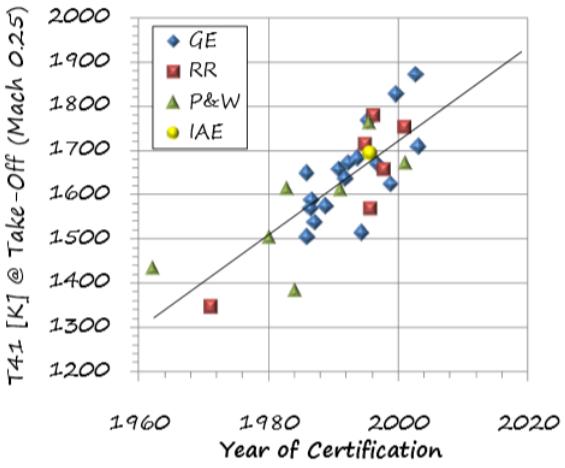

(b) *TIT as a function of certification year*

Figure 1.1.2: *Overall pressure ratio and turbine inlet temperature as a function of certification year [2]*

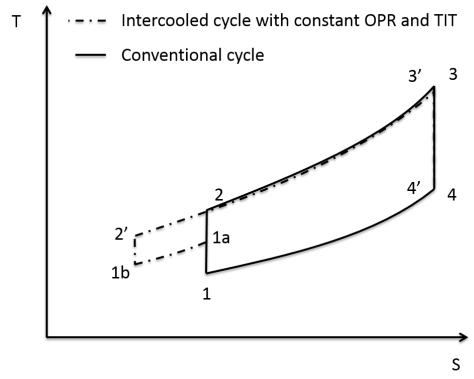

(a) *Intercooled cycle with constant OPR and TIT*

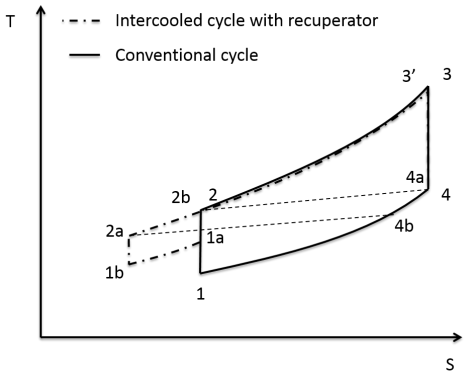

(b) *Intercooled cycle with recuperator*

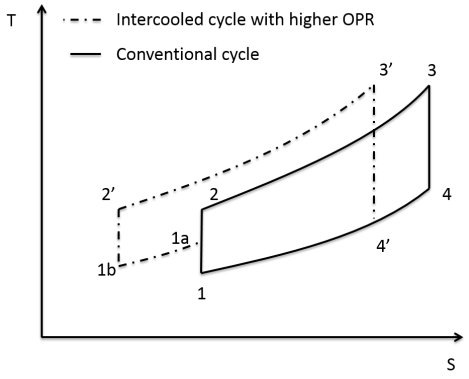

(c) *Intercooled cycle with higher OPR*

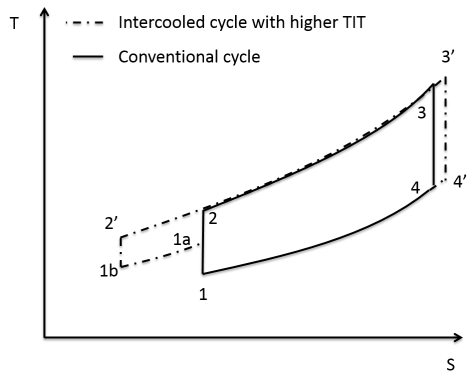

(d) *Intercooled cycle with higher TIT*

Figure 1.2.1: *Intercooled cycles illustration*

relaxed and a recuperator maybe favourable.

As the gas turbine technology has developed to modern times, the turbine cooling and the material technology has become an obstacle for designing gas turbines with higher OPR and TIT. Intercooling therefore draws a lot of attention because it could provide a shortcut to enable higher OPR or TIT by cooling the high HPC delivery temperature. Illustrations of these two options are shown in Figure 1.2.1c and Figure 1.2.1d. One can also choose to increase both the OPR and TIT with the benefit of intercooling. Meanwhile, more advanced and compact heat exchanger designs give more opportunities implementing the intercooling technology in mobile gas turbines.

1.2.1 Intercooling for stationary and marine gas turbines

As early as the 1950s, the world first fully gas turbine-powered ship HMS Grey Goose was launched. The heart of which was the Rolls-Royce RM60 as shown in Figure 1.2.2, a gas turbine with intercooling and a recuperator. In late 1990s, still Rolls-Royce, incorporated intercooler and exhaust heat recuperator to their advanced marine gas turbine engine WR-21. This engine was announced that it could offer up to 30% reduction in fuel burn compared to the existing simple cycle gas turbines for typical ship operating profiles.

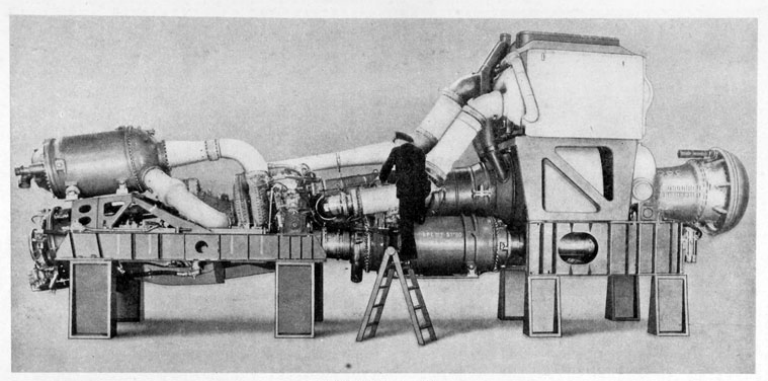

Figure 1.2.2: *Rolls-Royce RM60 marine gas turbine [3]*

For stationary applications, the most successful modern intercooled gas turbine is the General Electric LMS100. It is reported to reach the highest simple cycle efficiency of 46% in the industry today. The use of intercooling gives the 3-spool gas turbine a cycle pressure ratio of 42 and a firing temperature of 1380 ^{o}C, which are much higher than that of other industrial gas turbines. The thermal efficiency of GE's second most efficient simple cycle gas turbine, the LM6000, is 42.7% operating at an OPR of 28.5.

One interesting thing that should be noticed here is that, for the gas turbines mentioned above, they are all aeroderivative gas turbines.

1.2.2 Intercooling for aero engines

As intercooling has been successfully supplied to the stationary and marine gas turbines, in recent aero engine core concept development, it has been seriously considered as a key potential for higher energy efficiency and low emissions. In more detail, it is believed that applying intercooling to aero engines could provide the following benefits [4, 5]:

- Lower cooling air temperature by lowering the HPC delivery temperature. The lowered cooling air could ease the cooling requirement and hence release the OPR and/or TIT limit.
- Smaller engine core size through increased specific thrust level. Higher BPR could be achieved.
- By reducing the compressed air temperature, the later compression work required can be reduced. This could also help to achieve a higher OPR.
- Reduced NO_x emissions through reduced combustor flame temperatures.

However, unlike the stationary and marine gas turbines, which allow the use of a bulky intercooler installation, it is particularly important to achieve a compact intercooler design for aero engine applications. Increasing the volume requirement may lead to an increase in maximum engine diameter and add to installation losses through nacelle drag. Increased volume may also negatively influence pressure losses associated with the intercooler installation, add to shaft lengths and in turn cause vibration problems. Additionally, increased engine weight will offset the fuel burn benefits from improved SFC.

To be able to optimize the performance of an intercooled aero engine, the performance characteristics of a given intercooler architecture has to be known in the parameter range anticipated for the aero engine optimization. Hence, although the design of compact heat exchangers is a mature field and a wealth of design data exists [6], the availability of data directly applicable to aero engine performance studies is quite limited. A particular intercooler system for aero engine application must then be established. At the same time of delivering adequate heat transfer at a sufficiently low pressure loss in the aero engine operation range, attention must be paid to the intercooler weight and volume.

In addition, as the intercooling could be positioned anywhere during the compression process, where to install the intercooler system is an important issue that has to be addressed. Generally speaking, an early introduction is favourable from a thermodynamic perspective whereas a later introduction will reduce the intercooler pressure losses, weight and simplify its integration by reducing the intercooler volume requirement.

Besides the consideration of the intercooler system, how to use intercooling during the operation of an intercooled aero engine for a flight mission is also a key to minimize the fuel burn. For a typical flight mission, different from stationary and marine applications, the ambient conditions for the aircraft is largely influenced by the flight altitude. Operating points such as take-off, top-of-climb (TOC) and cruise result in different working conditions for an aero engine, and hence also in a varying intercooling demand for an intercooled aero engine.

1.2.3 Some recent research projects on aero engine intercooling

Recent aero engine intercooling research projects have been concentrating on designing a compact and low loss intercooler system. For example, within the EU Framework 6 New Aero Engine Core Concepts (NEWAC) programme [7, 8], an annular zigzag arrangement of corrugated heat exchangers around the core was designed by Rolls-Royce UK and Oxford University with its ducting system designed and tested at Loughborough University. In order to maximize the benefit of the intercooled core, great efforts were devoted to minimize the installation penalty of the intercooler system [9, 10] and to reduce the pressure loss in the intercooler and its ducting system [11, 12]. The study of this intercooler initialized the aero engine intercooling research within the EU framework programme, and provided guidance for the intercooler system design. The NEWAC intercooled aero engine core configuration is shown in Figure 1.2.3.

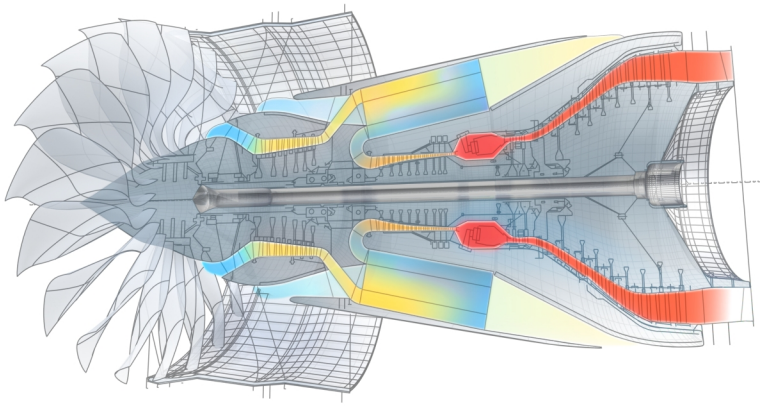

Figure 1.2.3: *NEWAC intercooled aero engine core configuration [13]*

Outside of the EU frame, the benefits from intercooling have also been realized. In the NASA N+3 SELECT vehicle study (Subsonic Fixed Wing Silent Efficient Low-Emissions Commercial Transport), compressor intercooling

for high-OPR engines was estimated to be at TRL 3 and the long term target (by 2020) for this project is a full-scale rig implementation for an aero engine with an OPR greater than 50 [14].

At the same time, with the spatial and weight considerations, Yutaka Ito et al. [15] at Tokyo Institute of Technology are trying to utilize the already existing components on the aero engine as heat exchangers for both intercooling and recuperation. For example, the compressor stators can be used as an intercooling section as illustrated in [15]. A method to evaluate this type of aerofoil heat exchangers has also been proposed by Yutaka Ito et al. [16].

1.3 Objectives of the work

The primary objective of this thesis is to build a systematic understanding of aero engine intercooling. The other objectives are:

- Complement the lack of open literature correlations on an aero engine intercooler system by providing the design, validation and results of the two-pass cross flow tubular intercooler.
- Provide validation for the design tool by verifying the CFD results with experiments.

2 Aero engine intercooler conceptual design

The layout of the intercooled core presented in this thesis is shown in Figure 2.0.1. A geared fan variant is adopted and the design strategy will be discussed in later chapter. The two-pass cross flow tubular intercooler, which is configured between the intermediate pressure compressor (IPC) and the HPC, was initialized by Chalmers University of Technology within EU projects NEWAC [17, 18] and fully established in Low Emission Core Technologies (LEMCOTEC) [19]. As shown in the right part of Figure 2.0.1, flow exiting an intermediate compressor or high speed booster enters the inflow duct through which it is diffused. The flow then enters the first stack of a tubular intercooler located downstream in the cooling flow direction, returns to an upstream tubular intercooler and then continues to an accelerating duct leading to the high pressure compressor entrance. Bypass air flows over the external surfaces of the two tubular stacks to achieve the sought intercooling. Twenty-four identical intercooler modules are distributed annularly around the core in design.

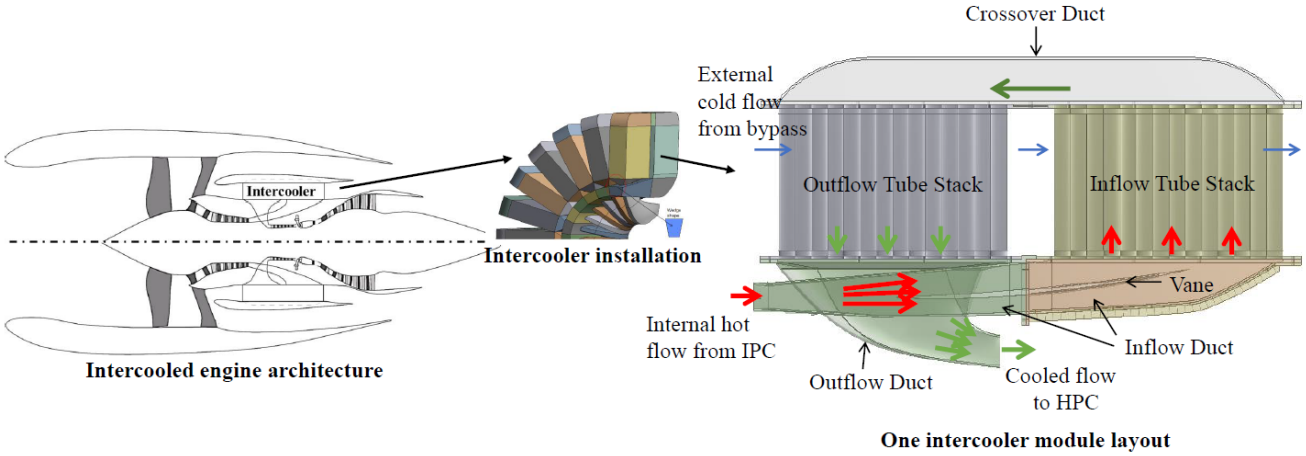

Figure 2.0.1: *Intercooler geometry and installation on aero engine*

As has been discussed in the introduction, a particular intercooler design for aero engine applications must be sufficiently compact, light and efficient in the aero engine operation range. To be able to achieve the targets, for the given two-pass cross flow tubular architecture, major considerations have been made for the tube stack configuration, tubes arrangement, associated ducts aerodynamic performance and flow distribution within tube stacks, as described below. In addition, optimization of the intercooler parameters, such as the tube size, the tube length and the number of the tubes is discussed. The CFD tool is briefly introduced here in this chapter as it is the main tool of shaping the design and establishing the correlations with the tube stacks modeled by porous media.

2.1 Selection of the tube stack configuration

Three different configurations for the two-pass cross flow intercooler have been considered. They are the straight tube (Figure 2.1.1a), the involute spiral (Figure 2.1.1b) and the U-bent involute spiral (Figure 2.1.1c). Obviously, the straight tube configuration has the simplest geometry and the easiest access for installation and maintenance. However, it gives the lowest space utilization and results in a relatively large nacelle for a given heat transfer area requirement. Also, because of the inefficient space usage, the frontal area for the intercooler external side cold flow is small and this results in a relatively large loss.

The involute spiral concept was developed to provide a better space utilization in comparison with the straight tube configuration. The tubes are bent following an involute spiral track which can be designed to fully occupy the space where the tubes extend. With this improvement in space utilization one can choose to reduce the length of the intercooler in the axial and/or the radial direction, to decrease installation volume required and/or to reduce

the incurred pressure loss. Frontal area of the intercooler is increased and hence a lower loss on the external side is obtained. In addition, comparing to the straight tube, the internal side of the bent tube is considered having a higher heat transfer and loss coefficient due to secondary flow effects.

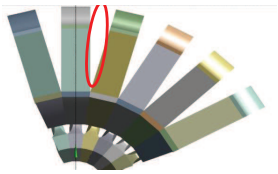

(a) *Staright tube configuration*

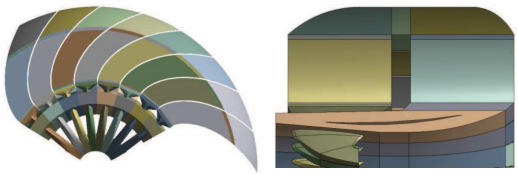

(b) *Involute spiral configuration*

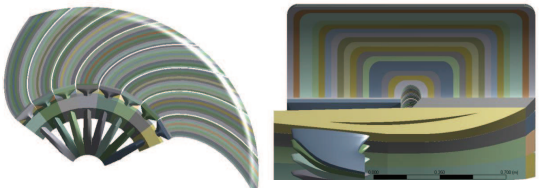

(c) *U-bent involute spiral configuration*

Figure 2.1.1: *Tube stack configurations*

The U-bent tube configuration creates a part of a counter flow pass which could increase heat transfer capability compared to the cross flow pass. As shown in Figure 2.1.1c, the crossover duct is replaced by a direct tube-to-tube connection, which leads to a more efficient space utilization. Without the crossover duct, the losses incurred by the sudden exit (tube stack to duct) and the sudden entry (duct to tube stack) can be reduced. However, the initial study shows that the flow mal-distribution of this concept is relatively severe because the length of the tubes varies substantially. One solution to this could be to use a varying tube diameter to offset the effect. More importantly, the size of tubes maybe very small to achieve a large wetted area for the intercooler. The U-bent combined an involute spiral shape of such a tube stack could be very expensive and difficult to be manufactured for a high pressure and temperature operation.

Taking both the considerations of space utilization and cost, the involute spiral configuration was adopted in all the intercooled engine assessments presented in this thesis. However, the associated duct aerodynamics design, and the experimental validation of the intercooler were based on the straight tube configuration because of its simplicity. More details will be given in the chapter covering the experimental work.

2.2 Selection of the tubes arrangement - intercooler external side

An aspect ratio of 8.0 is selected for the elliptical shape tubes within the study. With this aspect ratio, the relatively flat tubes give almost twice the wetted heat transfer area (perimeter x tube length) compared to a circular tube geometry having the same cross sectional area. Furthermore, the heat transfer capability of elliptical cylinders increases rapidly from an aspect ratio around 2.0 to up to around 8.0. After aspect ratio 8.0 there is only a limited improvement observed [20]. One thing that should be noted is, that the pressure difference between

the intercooler internal and the external sides may be very large depending on the IPC delivery pressure. There is a risk of deformation for the tubes during operation. In case of that, a manufacturing process for this type of tube described by MTU [21] is suggested. It is believed that the tube geometry can be produced in such a way that it will maintain its shape during operation.

Apart from the aerodynamic shape of the elliptical tube, the effect of different tube arrangement, in terms of inter-tube spacing, also needs to be explored. A schematic sketch of the problem configuration and an overview of the computational domain are shown in Figure 2.2.1. The range for the d_a and d_b parameters are given in Table 2.2.1. A more extensive parameter range has been explored and it has been found that going above $n = 1$ or $m = 3$ generally reduces intercooler performance by increasing size, volume and weight. Below $n = 0.75$ and $m = 1.0$ it is difficult to achieve low losses for the relatively large mass flow needed to obtain a sufficient amount of exchanged heat. 2D CFD was performed to establish pressure loss and heat transfer characteristics of each arrangement. To cover the anticipated range for all the mission points to be studied, correlations were made through a Reynolds number range of $10,000 < \mathrm{Re} < 120,000$.

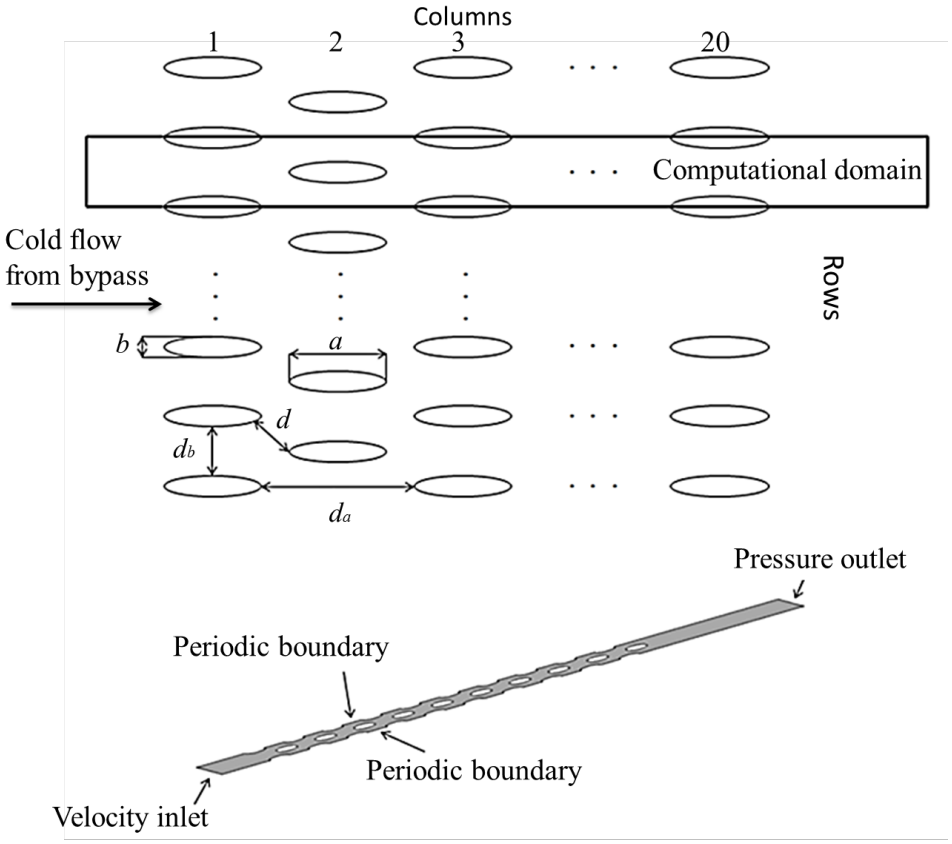

Figure 2.2.1: *Intercooler external side cross-section demonstration*

Distance along the external side flow direction $d_a = n \cdot a$	$n = 0.75, 0.8786, 1$
Distance along the transversal direction $d_b = m \cdot b$	$m = 1, 2, 3$
Ellipse aspect ratio	$a/b = 8/1$

Table 2.2.1: Intercooler external side parameter range and boundary conditions

For the evaluation of the heat transfer and aerodynamic properties of the external side of the intercooler the dimensionless heat transfer coefficient, the Colburn j factor, is introduced [6]:

$$j = St \cdot Pr^{2/3} = \frac{Nu}{Re \cdot Pr} \cdot Pr^{2/3} \tag{2.2.1}$$

The Nusselt number, the Reynolds number of the flow field and related hydraulic diameter are calculated from the expressions suggested by Kays and London [6]:

$$D_h = \frac{4A_cL}{A_w} \; ; \quad Nu = \frac{hD_h}{\kappa} \; ; \quad Re = \frac{(\dot{m}/A_c) \cdot D_h}{\mu} \tag{2.2.2}$$

where h is the local heat transfer coefficient; D_h is the hydraulic diameter of the flow field; k is the thermal conductivity of air; A_w is the surface area of the ellipses; A_c is the minimum flow cross sectional area and L is the total flow length of the intercooler. The friction factor f is defined through [6]:

$$\Delta p = \frac{(\dot{m}/A_c)^2}{2\rho_i}[f\frac{A_w}{A_c}\frac{\rho_i}{\rho_m} + (1+\sigma^2)(\frac{\rho_i}{\rho_o} - 1)] \tag{2.2.3}$$

where ρ_i and ρ_o are the fluid inlet and outlet density, ρ_m is the average of ρ_i and ρ_o, σ is the ratio between the minimum flow cross sectional area A_c and the intercooler frontal area A_f, and $\dot{m}$ is the mass flow at the inlet. In this equation the friction factor f represents an equivalent shear force per unit area in the flow direction composed of the true viscous shear forces as well as the pressure forces.

On the external side of the two-pass cross flow intercooler, the pressure loss incurred over the tube stacks is necessary to generate the heat transfer. A trade-off between heat transfer and pressure loss must be established in order to determine the optimal intercooler design. Going to higher levels of pressure loss has the drawback that fluid acceleration due to reduced stagnation pressure and heat addition tend to drive the loss levels up quickly [22] for a relatively modest gain in heat transfer, while lower pressure loss levels require excessive volume or tend to make the heat transfer insufficient.

2.3 Aerodynamic considerations - intercooler internal side

On the internal side of the intercooler, the pressure loss introduced inside of the tubes is also necessary to generate the heat transfer. On the other hand, the relatively large losses in the ducts do not contribute to the heat transfer. Pressure loss of this kind should be minimized and great care has therefore been taken to the losses occurring in the connecting ducts. Moreover, the flow distribution through the tubes should be considered as an important criterion for the connecting ducts design. As a uniformly distributed flow through the tube stacks gives the lowest average velocity in the tubes for a required heat transfer, the lowest pressure loss could be obtained.

2.3.1 Inflow duct design

As illustrated in Figure 2.0.1 the inflow duct of the intercooler is connected to the IPC exit and the tube stack interfaces. For conventional installations IPC exit Mach numbers are typically in the range of 0.25-0.35. Optimal Mach numbers inside of the tubes for this installation have been defined to be around 0.08 [23], which is a trade-off between the intercooler installation size and the loss incurred inside of the tubes. From the inflow duct entrance up to the tube stack, diffusion is hence needed to provide a flow speed adequate for the inflow tube stack. This diffusion, is quite challenging to achieve and this requirement leads to the introduction of guide vanes in the inflow duct.

For the studied intercooler concept, a counter two-pass configuration is used, see Figure 2.0.1. As heat is exchanged from the internal hot side to the external cold side of the intercooler, the temperature of the cooling flow increases in the flow stream direction. At the same time the temperature of the internal flow decreases. By positioning the inflow tube stack downstream of the outflow tube stack in the cooling flow direction, the temperature difference between the internal hot flow and the external cold flow as well as the amount of heat

transfer is balanced. However, the layout of a counter two-pass configuration results in an intersection between the inflow duct and the outflow duct, as shown in Figure 2.3.1.

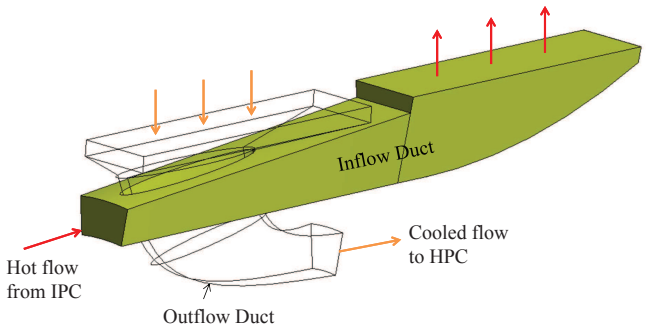

Figure 2.3.1: *Intersection between inflow duct and outflow duct*

The geometry parameters of the intercooler are determined in Figure 2.3.2a, normalized by the tube stack length l. The area ratio A2/A1 is 1.98 and A3/A1 is 11.3. As shown in Figure 2.3.2b, the area variation along the inflow duct shows a quite aggressive area change due to the presence of the intersection. Separation can easily occur just downstream of the intersection in the inflow duct. To control the flow in this region, an inflow guide vane is introduced as described in Figure 2.3.3.

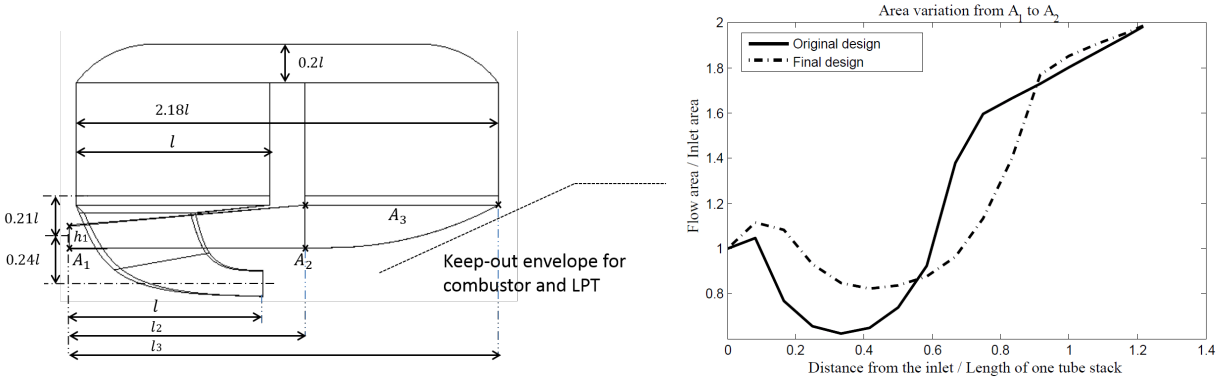

(a) *Intercooler geometry parameters* (b) *Area variation along inflow duct*

Figure 2.3.2: *Intercooler geometry parameters and area variation along inflow duct*

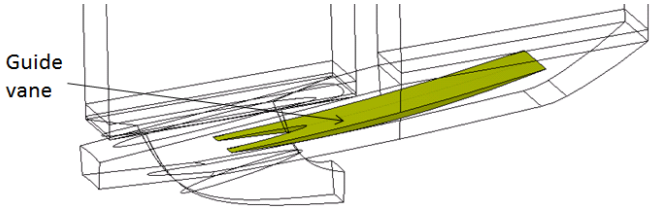

Figure 2.3.3: *Inflow duct guide vane*

2.3.2 Crossover duct design

As a bridge of connecting the two tube stacks, the pressure loss incurred in the crossover duct is marginal because of the relatively low flow Mach number. Compared to the introduced loss, the influence of the crossover duct on the flow distribution within the tube stacks is more critical. As demonstrated in Figure 2.3.4, flow inside of the crossover duct can be visualized. As the flow exits from the inflow tube stack, more and more flow merge on the way approaching the outflow tube stack which gives a higher velocity and lower pressure. After the mid region, flow is distributed to the tubes within the outflow tube stack and an adverse pressure gradient is established. In the presence of this duct, the flow distribution with the tube stacks is hence a combined effect of the pressure distribution developed in all the ducts. It is viewed that the evaluation for the entire intercooler system is necessary to capture these coupled effects.

In addition, because of the adverse pressure gradient built in the region connecting with the outflow tube stack, flow separation is expected at the left corner of the crossover duct. A crossover duct vane and a splitter was introduced to help eliminating the separation as described in Paper B.

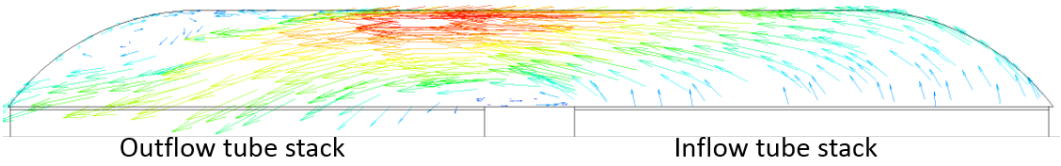

Figure 2.3.4: *Crossover duct flow demonstration*

2.3.3 Outflow duct design

As mentioned in the inflow duct design section, the intercooler layout results in an intersection between the inflow and outflow ducts. A trade-off has to be made between the two for the limited space available. A first estimation has shown that the loss incurred in the inflow duct can be as high as three times of the loss in the outflow duct. Hence the considerations made were inclined to ease the inflow duct design.

From Figure 2.3.1, it can be seen that the cross-section of the outflow duct is of elliptical shape to achieve a smoother area variation in the inflow duct. After the intersection, the outflow duct needs to converge the flow to the entry of the HPC as shown in Figure 2.0.1, at the same time make a nearly 90 degree turn of the flow. From the long and narrow elliptical cross-section to the square-like entrance, within the relatively short distance, it is extremely difficult to achieve a low loss design with a uniform discharge. In this thesis, the outflow duct of the designed intercooler shows an acceptable level of loss but with some flow distortion at the exit. Adjustment of the HPC installation position may be required to support a better design.

2.4 CFD Design tool

The CFD computations within this work were all performed using Ansys CFX [24, 25]. Meshes were generated by Ansys Meshing [24]. The shear stress transport (SST) turbulence model is adopted here, which has shown to give reasonably good predictions of separation and possible flow recirculation modelling [26, 27].

At the early stage of the development for a heat exchanger, porous media CFD has been applied frequently as a relatively convenient and inexpensive approach. The porous media can be setup to accurately reflect the macroscopic characteristics of the complex heat transfer units, without resolving internal flow details. A similar type of tubular heat exchanger was used as an aero engine recuperator by MTU. The studies of this recuperator have been performed numerically and experimentally by Aristotle University of Thessaloniki. A porous media model was developed to correctly describe the thermal and flow characteristics of the heat exchanger units [28, 29, 30]. With the established porous media model, the arrangement of the recuperator matrices was simulated and optimized [31].

In this work, the introduction of the porous media model for calculating properties of the internal side intercooler tube stacks allows realistic loss modelling when calibrated. The advantage is that the entire intercooler can be treated in a single three-dimensional simulation allowing interactions between the connection ducts and the

intercooler tubes to be studied at an affordable computational effort. This is a quite valuable approach since the pressure losses in the intercooler tubes strongly influence the flow distribution in the connection tubes and conversely any flow mal-distribution will have a strong effect on the pressure loss distribution in the intercooler tubes.

The porous media simulations are based on the Darcy pressure drop law, set up with a directional pressure loss model. The stream-wise directional loss is determined by the quadratic resistance coefficient k' , see [24], defined as:

$$\frac{\Delta p}{\Delta x} = -k' V|V| \tag{2.4.1}$$

where V is the true velocity of the flow assuming an even flow distribution, and Δp is the pressure loss along tube with length Δx. To keep the stream-wise direction to be the unique flow direction, the transverse directional loss coefficient is increased. Here a factor of 100 provided good control over the flow direction within the tubes.

2.5 Other intercooler design parameters

During the optimization of an intercooled engine the following design parameters have to be known to be able to setup the geometry of the intercooler: the tube size, the tube length, the number of the tube rows and the number of columns. Generally, the optimization of these parameters is a trade-off between aerodynamic loss and compactness.

2.5.1 Selection of the tube size

As the size of the tube decreases, the total perimeter length of the tubes increases for a given cross sectional area which leads to an increase in the wetted area and compactness of the intercooler. On the other hand, a smaller size of the tube would result in a lower Reynolds number which gives a higher friction factor.

With a sufficiently small tube diameter, the Reynolds number inside the tubes will even drop into the the laminar flow region. In the laminar flow regime, the internal local heat transfer coefficient shows a rapidly increasing behaviour with decreasing tube diameter [32]. To decrease the diameter of the flow passage well into the laminar regime, targeting a micro-channel heat exchanger design, has the potential of having the heat transfer surface density as high as 10 times the conventional compact heat exchanger. However, for intercooling applications, the relatively large amount of mass flow introduces a substantial challenge with respect to the high flow friction factor and the associated high Mach numbers.

2.5.2 Selection of the tube length

The main advantage of an increased tube length is the reduction in the intercooler external side pressure loss through a larger frontal area, which gives a lower flow Mach number through the intercooler external side. One can also reduce the number of the tubes to further decrease the loss as the increase of the tube length gives more heat transfer area. A demonstration of the intercooler tube length is given in Figure 2.5.1. However, the drawbacks of a longer tube design frequently dominate. Firstly, even though the larger frontal area could give a lower external side loss, the diffusion for extracting the cooling flow from the bypass to the intercooler external side at the same time gets more difficult. Secondly, the tube length has a limitation of keeping the external bypass flow Mach number and the nacelle maximum diameter down. Longer tubes could push the nacelle diameter to a higher value which gives more drag. Thirdly, a longer tube introduces more pressure loss in the internal side of the tubes. Previous studies have shown that the internal side pressure loss of the intercooler is more critical than that of the external side.

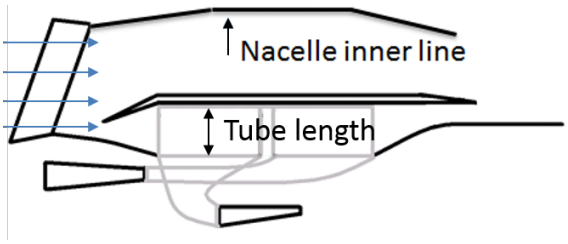

Figure 2.5.1: *Intercooler tube length denmonstration*

2.5.3 Selection of the number of tube rows and columns

The estimation of the number of tube rows and columns in the two intercooler stacks requires an iterative design process. Since the mass flow, temperature and pressure at the intercooler internal side inflow are given from engine boundary conditions, the assumption of a Mach number on the internal side of the tubes will lead to an estimate of the total internal flow area. For a given tube diameter the required number of tubes can then be calculated. Having defined the location of the intermediate and high pressure compressor interfaces as well as the available radial space for installing the intercooler, the total number of tube rows around the circumference can be estimated. This then allows the calculation of the number of tube columns. The rows and columns of the intercooler tubes are defined in Figure 2.2.1.

For a certain number of tubes, the distribution between the number of rows and the number of columns also plays an important role in the intercooler performance. With a given single tube size and heat transfer area, fewer columns are desirable for decreasing the external side pressure loss. A high radius installation of the intercooler gives more rows and fewer columns but also increases the nacelle diameter.

2.6 Correlations

This section provides a set of correlations useful for system evaluations of the straight and involute spiral configurations. The results are established by a series of parametric variations and evaluated based on expressions previously defined in this thesis and Paper B.

2.6.1 Intercooler external side

The correlations provided below are valid in the range of $10,000 < \mathrm{Re} < 120,000$. The largest deviation from CFD data is 0.90%.

Case A: $d_a = a$**, and** $d_b = b$

$$j = 0.00397e^{-0.0001144Re} + 0.003159e^{-4.427\cdot10^{-6}Re} \tag{2.6.1}$$

$$f = 0.01193e^{-0.0001305Re} + 0.008503e^{-5.292\cdot10^{-6}Re} \tag{2.6.2}$$

Case B: $d_a = a$**, and** $d_b = 2b$

$$j = 0.003469e^{-7.117\cdot10^{-5}Re} + 0.003461e^{-3.793\cdot10^{-6}Re} \tag{2.6.3}$$

$$f = 0.01044e^{-6.806\cdot10^{-5}Re} + 0.008109e^{-2.908\cdot10^{-6}Re} \tag{2.6.4}$$

Case C: $d_a = a$**, and** $d_b = 3b$

$$j = 0.003402e^{-5.241\cdot10^{-5}Re} + 0.003417e^{-2.739\cdot10^{-6}Re} \tag{2.6.5}$$

$$f = 0.009905e^{-5.162\cdot10^{-5}Re} + 0.009003e^{-2.303\cdot10^{-6}Re} \tag{2.6.6}$$

Case D: $d_a = 0.8786a$**, and** $d_b = 2b$

$$j = 0.002967e^{-6.734\cdot10^{-5}Re} + 0.00329e^{-3.385\cdot10^{-6}Re} \tag{2.6.7}$$

$$f = 0.009581e^{-6.043\cdot10^{-5}Re} + 0.009015e^{-1.617\cdot10^{-6}Re} \tag{2.6.8}$$

Case E: $d_a = 0.75a$**, and** $d_b = 2b$

$$j = 0.003328e^{-8.018\cdot10^{-5}Re} + 0.003389e^{-4.338\cdot10^{-6}Re} \tag{2.6.9}$$

$$f = 0.009929e^{-6.404\cdot10^{-5}Re} + 0.007792e^{-6.163\cdot10^{-7}Re} \tag{2.6.10}$$

2.6.2 Intercooler internal side

Inflow duct (Reynolds number based on the inflow duct inlet condition, valid in the range of 500,000 to 1,400,000, and the largest deviation in this correlation is 0.81%)

$$K_{inflowduct} = -1.626 \cdot 10^9 Re^{-1.837} + 0.5513 \tag{2.6.11}$$

$$K_{inflowduct} = \frac{p_{out} - p_{in}}{P_{in} - p_{in}} \tag{2.6.12}$$

Tube (Loss correlation[33], Heat transfer correlation [34])

$$\frac{1}{\sqrt{k_{loss}}} = -1.8\log_{10}(6.9/Re + (\epsilon/D/3.7)^{1.11}) \tag{2.6.13}$$

$$Nu = (\frac{(k_{loss}/8.0)(Re - 1000)\cdot Pr)}{1 + 12.7\sqrt{k_{loss}/8.0}(Pr^{2/3} - 1)} \tag{2.6.14}$$

Crossover duct (Reynolds number based on the crossover duct inlet condition, valid in the range of 100,000 to 350,000, and the largest deviation in this correlation is 0.78%)

$$K_{crossoverduct} = 3.128 \cdot 10^{-7} Re + 10.1 \tag{2.6.15}$$

$$K_{crossoverduct} = \frac{p_{in} - p_{out}}{P_{in} - p_{in}} \tag{2.6.16}$$

Outflow duct (Reynolds number based on the outflow duct outlet condition, valid in the range of 1,500,000 to 5,500,000, and the largest deviation in this correlation is 0.72%)

$$K_{outflowduct} = 1.939 \cdot 10^{11} Re^{-2.1} + 0.08107 \tag{2.6.17}$$

$$K_{outflowduct} = \frac{P_{out} - P_{in}}{P_{out} - p_{out}}(Totalpressurelosscoefficient) \tag{2.6.18}$$

where in the correlations above, the K is the loss factor with the subscript representing which duct it applies to; p is the static pressure and P is the total pressure, while 'in' and 'out' subscript represents the inlet and outlet of the duct respectively.

3 Intercooled aero engines evaluation

Having established the correlations of the two-pass cross flow tubular intercooler, optimal intercooled engines can now be set up. With the selected engine architecture, the assumed design point performance parameters and the flight mission requirements described in this chapter, three optimal intercooled engines are introduced. The performance of which are compared with a reference non-intercooled engine to show the benefits of intercooling. In addition to the traditional performance analysis, quantitative details are given by the use of exergy breakdown analysis. Together with the intercooling control and an axial-radial compressor concept introduced below, the intercooled engines can be as high as 5.3% more efficient than the non-intercooled engine.

3.1 Engine performance evaluation tool

The Chalmers in-house engine performance code GESTPAN [35] was used to conduct the multipoint performance evaluation in this thesis. The output data from these simulations were used to carry out the conceptual designs using the Chalmers in-house code WEICO (weight and cost estimation). The WEICO program is a FORTRAN 90 implementation derived on principles similar to the ones presented in Ref. [36]. The WEICO code was developed and validated within the EU FP6 projects VITAL [37] and NEWAC [38] as well as extended within the FP7 project LEMCOTEC [23]. Details on its usage and methodology are presented in Refs. [39, 40].

3.2 Selection of the engine architecture

The selection of architecture for the intercooled engine is a result of two considerations. Firstly, as have been mentioned in the introduction, where to install the intercooler system is an important issue that has to be addressed. The optimal position in the compression process for the intercooler integration is dependent on the trade-off between the intercooler installation and the amount of heat rejected from the core. A bulky intercooler with high losses may be obtained if intercooling is introduced too early during the compression whereas a later introduction will increase the intercooler exergy destruction caused by the finite temperature driven heat rejection. To be able to explore a wider range of the integration, engine architectures suitable for intercooling would be either three-shaft, see Figure 3.2.1 or geared concepts, see Figure 3.2.2, which can be designed with a relatively high pressure ratio on the upstream compressor.

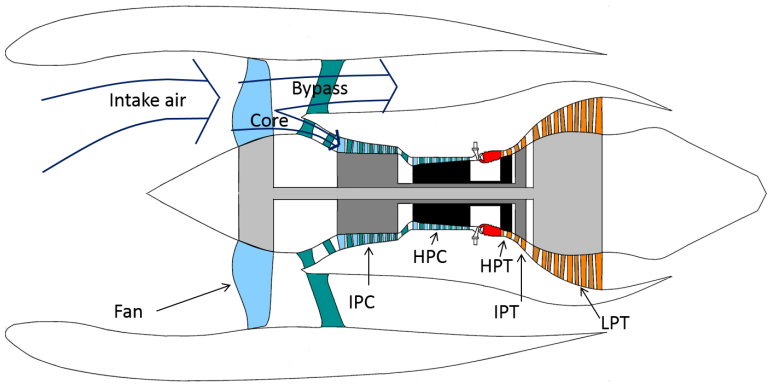

Figure 3.2.1: *Three shaft engine architecture*

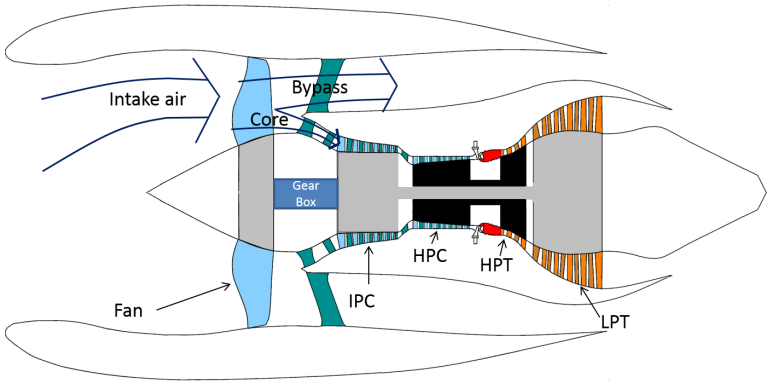

Figure 3.2.2: *Geared engine architecture*

Secondly, although a high HPC exit temperature arising from a high OPR can be avoided by intercooling, there is still a risk of an HPC efficiency drop due to a small blade height and a large hub/tip ratio [41]. A geared turbofan variant, is proposed to mitigate this effect [5, 23]. For a geared turbofan, the low pressure turbine (LPT) has a higher rotational speed than in the conventional turbofan, for which the rotational speed of the low pressure shaft is limited by the fan tip speed. The increased shaft speed allows for a smaller shaft diameter that makes it possible to integrate the HPC at a lower radius. This increases the last stage blade height. Furthermore, for the LPT, an increased rotational speed also gives a lower blade loading, higher efficiency and allows the use of fewer stages. The bypass ratio can be then ultra-high without an excessive number of LPT stages. The geared variant is therefore adopted for the study of intercooling in this thesis.

3.3 Design point performance parameters assumptions

Design point data and constraints common to the reference non-intercooled engine and the intercooled engines are summarized in Table 3.3.1 below. The data are based on estimates on performance levels achievable for an engine entering into service (EIS) year 2025. In order to establish optimal engines, pressure ratios of the compressors and BPR are varied while the constraints are mainly the HPC exit temperature (950 K) and the HPT rotor entry temperature (1900 K). The efficiencies in the table are polytropic. T_{blade} is the allowed maximum blade temperature. A hot day take-off condition is used to evaluate the engine at the start of the mission analysis. The cooling flow is then calculated based on the model established in [42].

Parameter	Value
$T_{HPC,exit}$	$< 950\ K$
$T_{HPT,rotor,entry}$	$< 1900\ K$
T_{blade}	$< 1210\ K$
η_{fan}	93.5%
η_{IPC}	92.2%
η_{HPC}	92.5%
η_{HPT}	90.7%
η_{IPT}	91.4%
η_{LPT}	93.25%
Design take-off net thrust	$291,900\ N$

Table 3.3.1: Design point performance parameters (take-off)

In addition to the parameters listed in the table above, during optimization the OPR may become limited also because the last stage HPC exit blade height value has reached the point where the HPC efficiency starts to drop off rapidly [41]. Even though the geared core is adopted here as discussed in previous section. A rule of thumb is that the compressor blade height should not be lower than 12 mm and the hub tip ratio should be kept lower than

0.92 to avoid end-wall boundary layer and tip leakage losses to become excessive. One solution to this problem is discussed later in this chapter exploring an ultra-high OPR intercooled engine by using an axial-radial compressor concept.

3.4 Mission optimization

The mission optimization procedure establishes an engine that provides minimum fuel burn for a fixed flight mission and fixed aircraft. The mission length is 6800 km. Initial cruise altitude is 35000 ft and final cruise altitude is 39000 ft. Airbus A330-300 is used as the aircraft model, which is a twin engine subsonic transport aircraft. The engine take-off net thrust is set to be 291,900 N which is considered suitable for the twin engine aircraft model. Detailed parameters can be viewed in table 3.4.1 as shown below.

Parameter	Value
Design mission range	$6,800\ km$
Take-off Mach number	0.21
Cruise Mach number	0.81
Maximum take-off weight	$176,000\ kg$
Initial cruise altitude	$10,668\ m$
Final cruise altitude	$11,887\ m$

Table 3.4.1: Mission optimization parameters

A factor of 1.5 is established to estimate the full fuel burn saving potential for a scalable aircraft. The reduced fuel consumption is attributed to the factors such as a more compact wing, fuselage load bearing structure, empennage and landing gear.

3.5 Intercooling control

As have been mentioned earlier in the introduction chapter, the ambient conditions during a flight mission are largely varied with different altitude. The challenge with achieving a high OPR is generally associated with the compressor outlet temperature for low altitude operations, such as hot day take-off and climbing. Colder fan inlet flow for higher altitude operation, such as cruise, results in a less demand for intercooling or even no intercooling. Studies have shown that the presented intercooler introduces considerable pressure losses in cruise (around 3-8% in the internal high pressure side and 7-10% on the external low pressure side). Intercooling also rejects heat from the core to the bypass which may reduce the thermal efficiency.

For an intercooled engine, a previous sensitivity study has observed that a 1% pressure loss reduction on the external low pressure side through intercooler can be translated to a 0.2% SFC reduction, while the effect of 1% pressure loss reduction on the internal high pressure side is stronger which equals to about 0.3% SFC reduction. Similar conclusions can be seen from [43, 44]. Therefore, a reduction of intercooling at the point when the demand of intercooling is marginal could be beneficial. In this section, two ways of controlling intercooling are introduced, named external side variable separate nozzle (VSN) for the coolant flow and internal side variable flow path (VFP) for the core flow.

3.5.1 Variable separate nozzle

Reducing the coolant mass flow reduces intercooler external Mach numbers and related pressure losses, both over the intercooler and in the upstream intercooler diffuser. The reducing of the coolant mass flow also decreases transferred heat, which leads to an increased combustor inlet temperature and a reduced fuel flow need. Generally, two options are available to achieve this control.

The intercooler may be integrated either allowing the internal bypass air to mix with the external bypass air, see upper part of Figure 3.5.1, or to be exhausted separately as indicated in the lower part of Figure 3.5.1. For the studied two-pass intercooler, there are two major problems of using the mixed nozzle. First is the problem

induced by the pressure match at the mixing plane. As it will be seen later in the results, the intercooler external pressure loss at take-off is around 15% to be able to achieve sufficient heat transfer. With this high pressure loss, a very high Mach number is required for the external bypass flow to match the low pressure of the internal bypass flow stream. Secondly, the engine performance is quite sensitive to the mixing loss of the mixer. An ideal mixing assumption will be too optimistic for the performance evaluation. The advantage of the auxiliary variable nozzle, compare to the variable mixer, is the freedom of control. The auxiliary nozzle is able to control the coolant mass flow by simply adjusting the nozzle area independently without the consideration of the mixing and associated loss. Hence, the separate nozzle was used in the intercooler external coolant flow control. A simple demonstration of the separate nozzle detail is given in Figure 3.5.2.

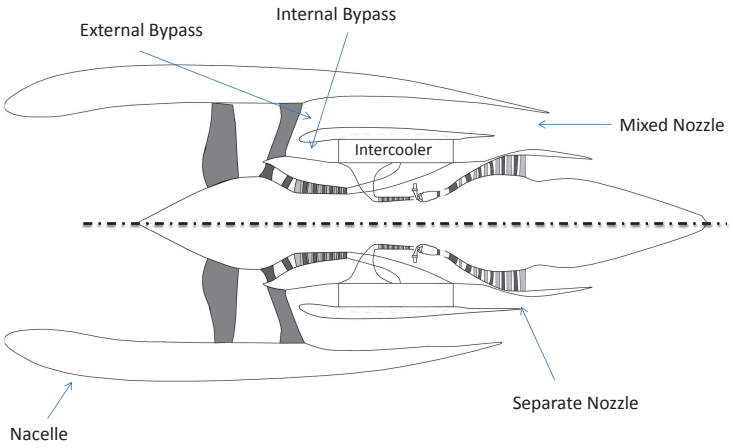

Figure 3.5.1: *Intercooled engine layout with mixed nozzle (upper) and separate nozzle (lower)*

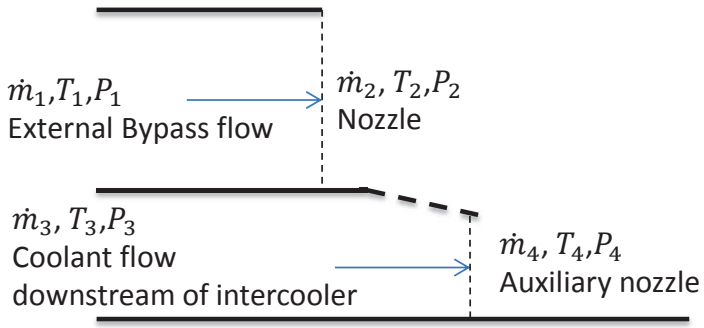

Figure 3.5.2: *Intercooler separate nozzle deomnstration*

3.5.2 Intercooler internal variable flow path

For the intercooler internal core side, the control of intercooling can be achieved through bypassing the core flow from the intercooler. A simple way of bypassing the flow is to add another duct to the intercooler ducting system, as can be seen in Figure 3.5.3. By opening the intercooler bypass duct at cruise for part of the core flow, the heat rejection from the core to the intercooler external side is further reduced together with the utilization of the separate nozzle. At the same time, the incurred pressure losses through the intercooler and ducts can be largely cut off. With the presence of the intercooler and its associated ducts, there is a limited space available for this additional intercooler bypass duct to be designed as a normal inter-compressor duct. To design the duct for part of the core flow would reduce the difficult of its integration. Moreover, bypassing all the core flow through the variable flow path would increase risk of intercooler icing problems at cruise, 35000/39000 ft altitude for the

studied mission. Part of the core flow is then needed to go through the intercooler tubes to avoid freezing.

However, a problem may arise due to the flow split. The flow streams through the intercooler bypass duct and the intercooler can have quite large temperature difference due to the intercooling effect. A temperature distortion of the outflow leaving the intercooler is then expected and it will influence the performance of the downstream HPC.

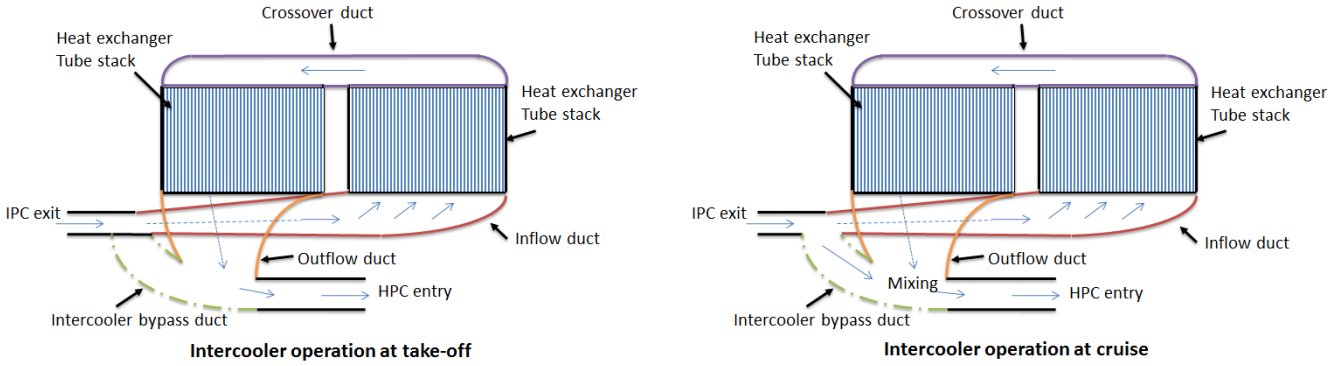

Figure 3.5.3: *Intercooler internal side variable flow path bypass duct*

3.6 Established engines

3.6.1 Non-intercooled reference engine

In order to show the benefit that the intercooler could bring, an advanced non-intercooled geared engine is modelled as the reference engine for comparison. The engine architecture can be viewed in Figure 3.2.2. The advanced non-intercooled geared engine is optimized by varying the bypass ratio, fan, IPC and HPC pressure ratio. The optimal OPR at take-off is found to be 55. A higher OPR is limited due to the compressor exit temperature and the increasing cooling flow requirement offsets the high OPR benefit.

3.6.2 Intercooled engine with VSN

Similar to the non-intercooled geared reference engine, the intercooled geared engine is also optimized by varying the BPR, the fan, the IPC, and the HPC pressure ratios. In addition, intercooler tube length, tube diameter, and tube internal Mach number are optimized simultaneously. After a number of preliminary optimization studies the following intercooler parameters were used as shown in Table 3.6.1.

Ellipse major axis length	30.7 mm
Number of tube columns per stack	20
Number of tube rows per stack	12
Number of tube stacks	2×24 (two pass)
Tube arrangement	Case B, m=2, n=1
Mach number in tube (take-off)	0.07
Tube length	0.37 m
Intercooler height	0.43 m
Intercooler length	1.3 m
Intercooler weight	306 kg
Intercooler configuration	Involute spiral

Table 3.6.1: Two-pass cross flow tubular intercooler parameters for the optimized intercooled geared engine

The optimal OPR at take-off for this intercooled engine is 79. An even higher OPR is constrained by the HPC

last blade height. As the modern aero engine HPC exit Mach number is in the range of 0.23-0.30 [45], to design the HPC with the lower bound would result in a HPC last blade height of 13.6 mm. While the design with the higher bound leads to a problematic blade height close to 10 mm [41].

As a part of the optimization, the intercooler coolant mass flow is being controlled by a separate variable nozzle as illustrated in the intercooling control section, see Figure 3.5.1 and Figure 3.5.2. The use of the separate nozzle can considerably reduce the irreversibilities associated with the coolant flow and limit the heat rejection from the core. However, the fan mass flow decreases when the auxiliary nozzle area is decreasing. Hence, the specific thrust level is going up and this deteriorates the benefit through a decreased propulsive efficiency. As shown in Table 3.6.2, an optimal point can be found where the decreased propulsive efficiency starts to active.

Cruise phase	Nozzle 100%	Nozzle 60%	Nozzle 30%	Nozzle 10%
OPR	79	76	74	73
Fan mass flow (kg/s)	406	393	382	374
Core flow temperature drop (K)	-84	-75	-59	-31
Coolant flow pressure loss	-23.5%	-11.7%	-3.8%	-0.55%
Coolant mass flow (kg/s)	39.5	28.2	15.0	5.0
Cruise SFC (mg/Ns)	13.41	12.85	12.68	12.72
Cruise $\eta_{thermal}$	0.509	0.532	0.542	0.543
Cruise $\eta_{propulsive}$	0.809	0.809	0.805	0.801

Table 3.6.2: Coolant flow control results

Notice that this behavior is opposite to how the engine reacts to a variable mixer (for which the total exhaust nozzle area will not change). For this configuration a reduced area for the coolant flow passage will reduce the pressure loss over the intercooler surface and so is the heat transfer, giving a lower temperature and higher stagnation pressure in the flow. To keep the corrected flow in the nozzle constant the mass flow must increase in the external bypass (assuming that the nozzle is choked in top-of-climb and cruise). Hence, a higher propulsive efficiency can be expected for the variable mixer.

3.6.3 Intercooled engine with both VSN and VFP

The intercooled engine with both a VSN and a VFP is established by keeping the key parameters the same as in the intercooled geared engine with a separate nozzle as described in the previous sub-section. The difference between the two engines is only that, with the VFP, the engine has the capability of bypassing part of the core flow from the intercooler. With the use of titanium and a thickness of 2.0 mm, a simplified assessment shows that the total increase in weight including the duct and associated control is about 25 kg, which is less than 1/10 of the intercooler installation.

The optimization of the intercooled engine with both the VSN and the VFP is to vary the mass flow through the VFP duct to find the minimum cruise SFC. The duct loss of the VFP bypass duct is estimated on the basis of the work in [46]. Momentum balance and the mass weighted average enthalpy method are applied to model the mixing of the two flow streams, see [35]. The mixing loss is assumed to be of the same magnitude as the loss in the duct. With the losses introduced by the additional duct and flow streams mixing accounted, as illustrated in Figure 3.6.1, there is an optimal split ratio around 1 observed, where the split ratio is the mass flow ratio between the flow through the VFP bypass duct and the intercooler at cruise. As the flow through the VFP increases, the engine benefits the most from the loss reduction through intercooler in the beginning, see Figure 3.6.2. However, the decrease in SFC becomes slower after split ratio 1 because the decreased loss through the intercooler is approaching the loss through the VFP duct; hence, no further significant improvement can be obtained. At the same time, the HPC entry temperature as shown in Figure 3.6.3 continues to rise at a steady pace, which increases the power requirement of the compressor and deteriorates the SFC benefit from reducing intercooling. The design criterion for the intercooler bypass duct is hence to provide a low pressure loss path for 50% of the core flow bypassing the intercooler at cruise.

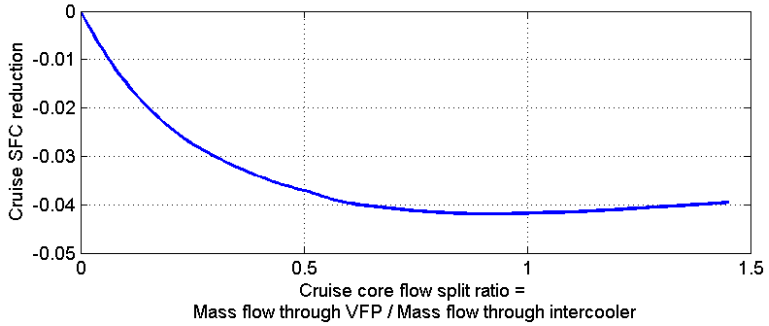

Figure 3.6.1: *SFC reduction for the intercooled engine with VSN and VFP when mass flow is varied through the VFP at cruise*

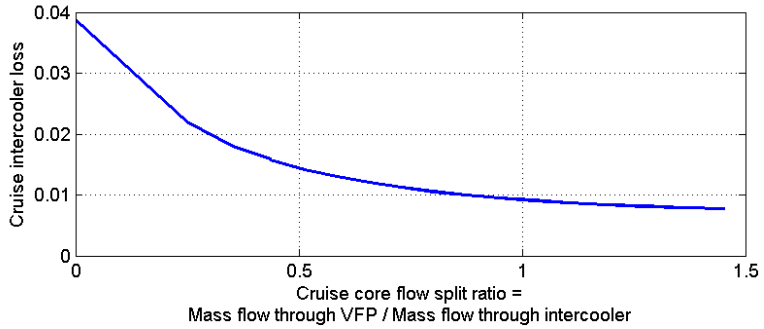

Figure 3.6.2: *Intercooler loss for the intercooled engine with VSN and VFP, varying mass flow through the VFP at cruise*

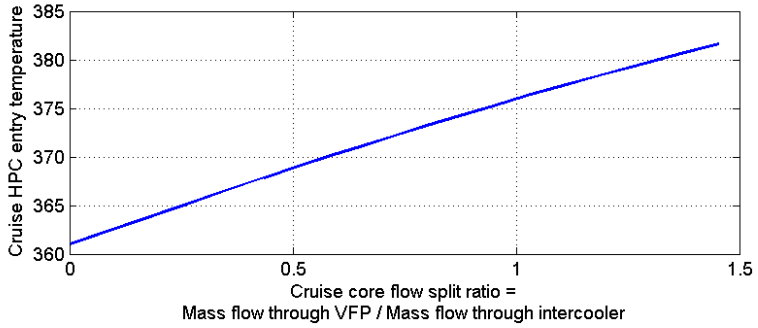

Figure 3.6.3: *HPC entry temperature for the intercooled engine with VSN and VFP, varying mass flow through the VFP at cruise*

3.6.4 Intercooled ultra-high OPR engine with VSN

As mentioned previously, the two intercooled engines established have achieved a limit of OPR set by the compressor exit blade height. Even though the geared variant is used and a low HPC exit Mach number is adopted, a maximum OPR at take-off has been found to be 79. To be able to further delay the constraint introduced by the last stage blade height, a reversed flow core engine was introduced in [41, 44]. With the low pressure shaft placed in tandem with the reversed flow gas generator, the concentric placement of the high pressure shaft is avoided. A even lower position than the conventional geared core for the high pressure system is hence achieved.

However, the delay of the constrain still has a limit. A full exploitation of intercooling is considered by introducing an axial-radial HPC design. Using a radial compressor in the later part of the HPC compression process would potentially provide a more efficient compression, through its more efficient handling of small volume flows without the consideration of the last blade height constrain. An example of the axial-radial HPC design for turbofan is given in Figure 3.6.4 within NEWAC project.

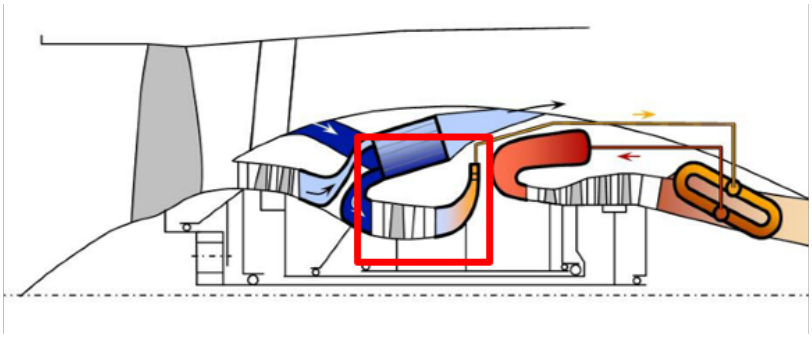

Figure 3.6.4: *Intercooled recuperative core with axial-radial HPC studied in NEWAC SP2, by PCA and MTU*

Generally, a lower efficiency for a radial compressor is expected than an axial compressor. The conceptual design studies carried out indicate that the last two axial stages should be replaced with a radial component. With the EIS year 2025 performance level assumption, a maximum efficiency of 91.5% was assumed for the radial part of the HPC compression (1% lower than the axial counterpart). A net efficiency for the entire HPC compression process was then assumed to be 92% for the IC ultra-high OPR axial-radial configuration. Apart from this change in the HPC polytropic efficiency, the optimization of this ultra-high intercooled engine configuration is identical to the optimization of the other two intercooled geared engines introduced earlier. As the optimal OPR at take-off for this engine is found to be 104, the highest OPR achieved is 140 at the top-of-climb (TOC) point. A BPR of 19.2 is obtained at take-off with a much lower optimal FPR than the other two intercooled engines. For this engine, a much larger fan diameter is expected for the low optimal FPR and high BPR. As the nacelle line moves radially with the change in intercooler size to keep the external bypass flow Mach number lower than 0.6, this engine hence allows an intercooler with a longer tubes. As discussed in the intercooler design section, longer tubes lead to a larger frontal area and a lower external side loss. Higher intercooler inlet pressure of this engine also results in a smaller number of tubes for the fixed Mach number inside of the tubes. A shorter intercooler is hence observed. The optimized intercooler parameters for this ultra-high OPR intercooled engine are shown in Table 3.6.3.

Ellipse major axis length	30.7 mm
Number of tube columns per stack	17
Number of tube rows per stack	12
Number of tube stacks	2×24 (two pass)
Tube arrangement	Case B, m=2, n=1
Mach number in tube (take-off)	0.07
Tube length	0.41 m
Intercooler height	0.46 m
Intercooler length	1.1 m
Intercooler weight	290 kg
Intercooler configuration	Involute spiral

Table 3.6.3: Two-pass cross flow tubular intercooler parameters for the optimized ultra-high OPR intercooled geared engine

3.7 Engine performance assessments

This section concludes all the optimal engines, including the engine architecture parameters, see Figure 3.7.1 and the engine performance data for the three operating points: take-off, see Figure 3.7.2; top-of-climb, see Figure 3.7.3; final cruise, see Figure 3.7.4. In general, lower fuel consumption is obtained by applying intercooling to the core. With a trade factor of 1.5, a net fuel burn reduction of 4.5% is observed for the intercooled geared engine with VSN compared to the non-intercooled geared concept. Further reduction in fuel burn, about 0.4% is achieved with a VFP concept. For the ultra-high OPR intercooled core engine, the use of an axial–radial compressor configuration results in a net fuel burn reduction of 5.3%. From the comparison of the detailed tradition performance data of these engines, followed comments can be made:

- With a constant TIT, the high OPR is the primary advantage of the intercooled cores. As mentioned many times in this thesis, this is achieved by the intercooled HPC inlet flow which reduces the HPC power requirement and the HPT cooling flow requirement. An ultra-high OPR core is accomplished with an axial-radial compressor to avoid the HPC efficiency drop due to a problematic last blade height. A higher OPR gives more expansion in the turbines which results in a lower temperature in the exhaust gas and improves the thermal efficiency.

- The higher BPR is another primary advantage of intercooled engines. As a lower core exhaust temperature has been achieved with higher OPRs for the intercooled engines, the optimal FPR is reduced in order to maintain an optimal velocity ratio [47]. Reducing FPR is followed by an increased fan diameter and an increased optimal BPR. For the intercooled engines with a lower HPC delivery temperature, such as the two intercooled engines with take-off OPR 79, the combustor temperature rise is larger for the constant TIT and therefore less core mass flow is required. In addition, lower cooling air temperature through a lower HPC delivery temperature demands less cooling flow need which also reduces the core mass flow need. All the effects described above drive a higher BPR for the intercooled engines and therefore a lower jet velocity and a higher propulsive efficiency as well as a lower jet noise is obtained.

- A pressure split exponent, n, which is defined as $n = log_{OPR}\frac{IPC\ delivery\ pressure}{Fan\ inlet\ pressure}$ [5], is used to show the optimal position during compression for the intercooling to be introduced. For the intercooled engines presented in this thesis, this exponent is relatively fixed. At top-of-climb, the exponents are 0.40, 0.40 and 0.41 respectively. Compared to a lower value of 0.38 estimated by Kyprianidis et al. [5] for a year 2020 intercooled core, the larger split exponent here is expected since the heat rejection is kept lower by the active use of the VSN at both TOC and cruise point. Therefore a later introduction of the intercooling is set to reduce the intercooler pressure losses, weight and volume requirements.

- One of the major drawbacks of intercooling is the pressure loss incurred through the intercooler components. The introduction of the variable separate nozzle and variable flow path concepts has largely reduced this side effect by turning the intercooling down when the demand is low.

- Sufficient heat transfer must be provided by the intercooler at take-off to enable the higher OPR restricted by the compressor exit temperatures for the advanced non-intercooled geared engine. Besides the increase of OPR and BPR, a large benefit is obtained from the reduced compressor exit temperature which gives a reduced cooling flow need. Less cooling flow will lead to less losses during not only take-off, but also the entire mission in HPT cooling.

- Potentially the reduced compressor exit temperature through intercooling could also be used to reduce NO_x emissions. Balance needs to be made between the fuel burn benefit and NO_X reduction.

	Advanced non-IC geared	Intercooled geared with VSN	Intercooled geared with VSN and VFP	Intercooled ultra-high OPR geared with VSN
Engine architecture	1-7-7-1-4	1-5-9-1-5	1-5-9-1-5	1-5-(7+1)-1-6
Engine weight (kg)	6957	6700	6737	7081
Nacelle diameter (m)	3.47	3.52	3.53	3.72
Nacelle length (m)	5.43	5.30	5.31	5.51
Mission fuel burn (kg)	base	-4.5%	-4.9%	-5.3%

Table 3.7.1: Optimal engine configurations for the studied mission

	Advanced non-IC geared	Intercooled geared with VSN	Intercooled geared with VSN and VFP	Intercooled ultra-high OPR geared with VSN
OPR	55	79	79	104
BPR	14.8	17.1	17.2	19.2
FPR (outer)	1.450	1.444	1.442	1.367
FPR (inner)	1.305	1.299	1.298	1.230
Fan mass flow (kg/s)	1343	1203	1207	1307
Main bypass duct pressure (kPa)	151.4	150.8	150.6	142.8
Main bypass duct temperature (K)	326	325	325	320
Core mass flow (kg/s)	87.3	68.2	68.1	66.4
IPC PR	5.42	4.98	4.98	5.90
IPC exit temperature (K)	527	514	514	533
HPC inlet pressure (kPa)	739.2	654.8	658.4	736.0
HPC PR	7.73	12.58	12.53	14.70
HPC exit temperature (K)	949	885	889	938
HPT inlet temperature (K)	1900	1900	1900	1900
HPT cooling bleed ratio	0.19	0.14	0.15	0.18
LPT inlet temperature (K)	1415	1417	1409	1351
Core nozzle exit temperature (K)	801	747	745	689
Intercooler core flow pressure loss	NA	3.0%	2.6%	2.9%
Intercooler core flow temperature change (K)	NA	-91	-95	-106
Intercooler VFP bypass mass flow (kg/s)	NA	NA	4.2	NA
VSN openess percentage	NA	100%	100%	100%
Intercooler coolant mass flow (kg/s)	NA	119	120	129
Intercooler coolant flow pressure loss	NA	12.0%	11.9%	11.4%
Intercooler coolant flow temperature change (K)	NA	52	50	54
SFC (mg/Ns)	8.25	8.16	8.12	7.69
$\eta_{thermal}$	0.501	0.501	0.499	0.496
$\eta_{propulsive}$	0.409	0.415	0.419	0.447

Table 3.7.2: Optimal engine performance data, take-off point

	Advanced non-IC geared	Intercooled geared with VSN	Intercooled geared with VSN and VFP	Intercooled ultra-high OPR geared with VSN
OPR	68	100	101	140
BPR	13.9	16.8	16.7	18.4
FPR (outer)	1.538	1.610	1.615	1.529
FPR (inner)	1.384	1.449	1.453	1.376
Fan mass flow (kg/s)	578	522	527	592
Main bypass duct pressure (kPa)	56.4	59.0	59.2	56.0
Main bypass duct temperature (K)	283	287	287	282
Core mass flow (kg/s)	39.8	30.3	30.6	31.4
IPC PR	6.30	4.31	4.36	5.45
IPC exit temperature (K)	481	439	441	464
HPC inlet pressure (kPa)	319.9	217.5	224.7	261.5
HPC PR	7.81	16.89	16.51	19.68
HPC exit temperature (K)	874	840	845	901
HPT inlet temperature (K)	1754	1918	1914	1932
HPT cooling bleed ratio	0.19	0.14	0.15	0.18
LPT inlet temperature (K)	1300	1428	1417	1371
Core nozzle exit temperature (K)	698	727	724	670
Intercooler core flow pressure loss	NA	4.9%	3.7%	4.8%
Intercooler core flow temperature change (K)	NA	-73	-79	-88
Intercooler VFP bypass mass flow (kg/s)	NA	NA	3.6	NA
VSN openess percentage	NA	60%	60%	60%
Intercooler coolant mass flow (kg/s)	NA	36.8	37.3	42.0
Intercooler coolant flow pressure loss	NA	8.4%	8.4%	8.8%
Intercooler coolant flow temperature change (K)	NA	59	56	65
SFC (mg/Ns)	13.08	12.95	12.86	12.49
$\eta_{thermal}$	0.555	0.574	0.573	0.576
$\eta_{propulsive}$	0.766	0.748	0.755	0.773

Table 3.7.3: Optimal engine performance data, top-of-climb point

	Advanced non-IC geared	Intercooled geared with VSN	Intercooled geared with VSN and VFP	Intercooled ultra-high OPR geared with VSN
OPR	52	74	75	105
BPR	15.6	18.9	19.0	20.6
FPR (outer)	1.388	1.452	1.457	1.394
FPR (inner)	1.249	1.307	1.311	1.254
Fan mass flow (kg/s)	436	380	383	434
Main bypass duct pressure (kPa)	42.0	43.9	44.1	42.1
Main bypass duct temperature (K)	271	275	276	272
Core mass flow (kg/s)	26.7	19.6	19.7	20.5
IPC PR	6.07	4.29	4.44	5.54
IPC exit temperature (K)	459	420	424	448
HPC inlet pressure (kPa)	229.3	163.1	174.5	202.4
HPC PR	6.87	13.73	12.98	15.76
HPC exit temperature (K)	808	783	803	848
HPT inlet temperature (K)	1552	1710	1727	1739
HPT cooling bleed ratio	0.19	0.14	0.15	0.18
LPT inlet temperature (K)	1147	1267	1273	1228
Core nozzle exit temperature (K)	609	637	643	593
Intercooler core flow pressure loss	NA	3.9%	1.2%	3.7%
Intercooler core flow temperature change (K)	NA	-59	-96	-72
Intercooler VFP bypass mass flow (kg/s)	NA	NA	9.7	NA
VSN openess percentage	NA	30%	30%	30%
Intercooler coolant mass flow (kg/s)	NA	14.4	14.9	16.5
Intercooler coolant flow pressure loss	NA	3.0%	3.0%	3.1%
Intercooler coolant flow temperature change (K)	NA	79	62	89
SFC (mg/Ns)	13.10	12.67	12.61	12.36
$\eta_{thermal}$	0.514	0.542	0.543	0.545
$\eta_{propulsive}$	0.822	0.807	0.808	0.822

Table 3.7.4: Optimal engine performance data, cruise point

3.8 Exergy analysis for aero engines

In the previous section, detailed traditional performance data of all the studied engines are presented. It has been discussed that the major benefits of intercooling are coming from the higher OPR and BPR, less cooling flow need, intercooling control etc. However, the quantitative details of these benefits were not described. To be able to quantify the benefits in a common currency, exergy analysis is briefly introduced in this section. Quantitative details are given in the form of exergy destruction breakdown.

3.8.1 Brief introduction of exergy analysis

Exergy is a measure of the available power of a flow stream. An aero engine is comprised of a series of interconnected open systems, such as compressors, turbines, nozzles and intercooler if intercooling is applied. By comparing the exergy of the inflows and outflows of an engine component and keeping track of component heat transfer, generated propulsive power and shaft power, a measure of component irreversibility is obtained. Combined the first and second laws of thermodynamics, see Kotas [48] and Horlock and Clarke [49] for a detailed description, the following inequality can be derived:

$$(\sum_i \dot{m}_i \varepsilon_i)_{in} \geq P_S + P_T - \sum_i \int \frac{T - T_\infty}{T} dQ_i + (\sum_i \dot{m}_i \varepsilon_i)_{out} \tag{3.8.1}$$

where the term on the left side is the mass flow associated inflow of exergy to the control volume. On the right of the inequality the last term represents the mass flow associated outflow of exergy to the control volume. P_S constitutes the shaft power transferred out of the control volume; P_T is the thrust power generated by the control volume; the third term captures heat transfer in of the control volume. The Equality only if all the processes in the control volume are reversible. The equation can be graphically visualized in Figure 3.8.1.

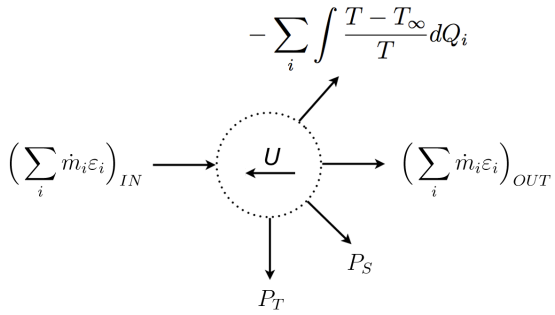

Figure 3.8.1: *Combined the first and second law of thermodynamics*

The specific exergy, ε, is calculated by the following equation:

$$\varepsilon = h - h_\infty + T_\infty(s - s_\infty) + \frac{C^2}{2} \tag{3.8.2}$$

where ∞ denotes the equilibrium condition, as defined through the ambient conditions of the environment. C is the absolute velocity and h is the static enthalpy. The irreversibility or exergy destruction per unit time, $\dot{I}$, is obtained from:

$$\dot{I} = (\sum_i \dot{m}_i \varepsilon_i)_{in} - (P_S + P_T - \sum_i \int \frac{T - T_\infty}{T} dQ_i + (\sum_i \dot{m}_i \varepsilon_i)_{out}) \tag{3.8.3}$$

The exergy destruction per unit time expresses the magnitude of the deviation from equality of Eq. 1, since under the assumption of reversibility equality holds and the exergy destruction per unit time is then zero. To establish normalized expressions for the exergy destruction per unit time as well as for the thrust power, the

specific exergy content of the fuel, ε_{fuel}, needs to be established. Assuming for a moment that this property is known, the normalized exergy destruction $\dot{I}$ can be formed according to:

$$\dot{I} = \frac{\dot{I}}{\dot{m}_{fuel}} \tag{3.8.4}$$

3.8.2 Exergy breakdown analysis comparison

Engine components exergy destruction for all the engines presented in this thesis are given here, see Figure 3.8.2, Figure 3.8.4 and Figure 3.8.6. By subtracting the reference non-intercooled engine data, the difference can be made more visible as shown in Figure 3.8.3, Figure 3.8.5 and Figure 3.8.7. Through the detailed quantitative data, it is viewed that a combined use of traditional performance and exergy breakdown analysis simplifies the analysis of complex engine systems. In general, following conclusions can be made:

- For all the engines studied, both non-intercooled and intercooled, the most inefficient components are the combustor and the nozzles.

- For the intercooled engines, the most significant effect is that it reduces the core nozzle exergy destruction. This is because of the higher OPR and a resulted lower core exhaust temperature.

- The second largest benefit is from the smaller core, which gives lower exergy destruction in combustor. At take-off, this can not be observed because the large amount of heat rejection during compression and the resulting higher temperature increase through combustion.

- The third most beneficial point of an intercooled engine is the less cooling flow need. This is shown in the HPT destruction for all the operating points.

- Intercooler incurred exergy destruction is detrimental according to the quantitative details. Intercooling control must be implemented to keep it low when the intercooling is not required.

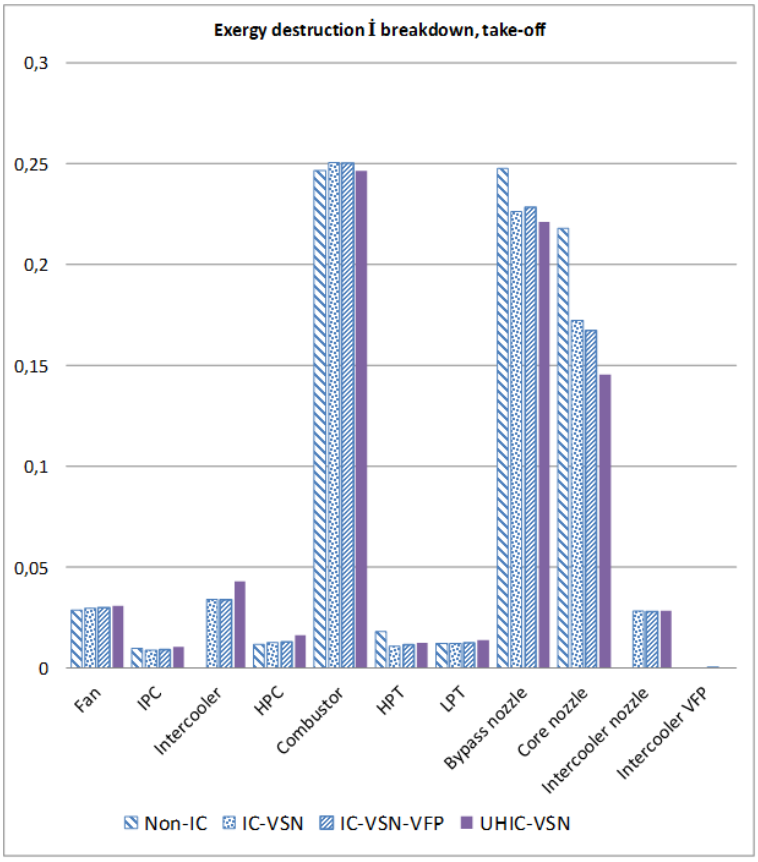

Figure 3.8.2: *Engine components exergy destruction per unit time, take-off point*

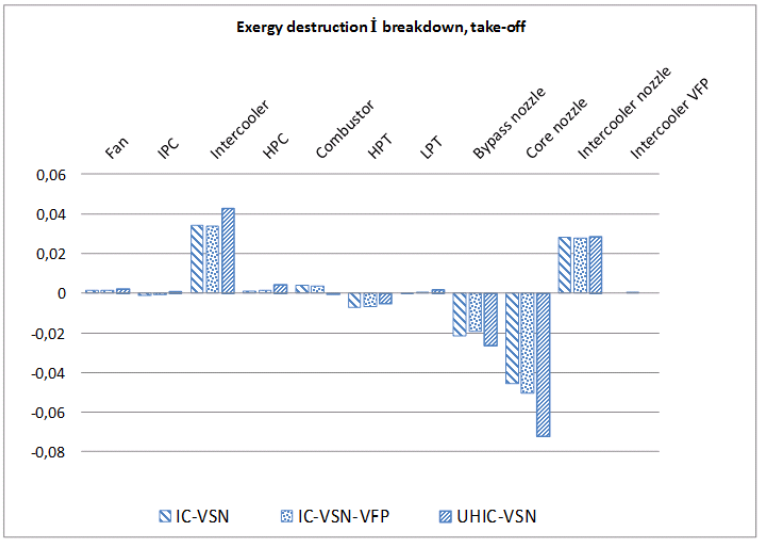

Figure 3.8.3: *Engine components exergy destruction per unit time subtract reference data, take-off point*

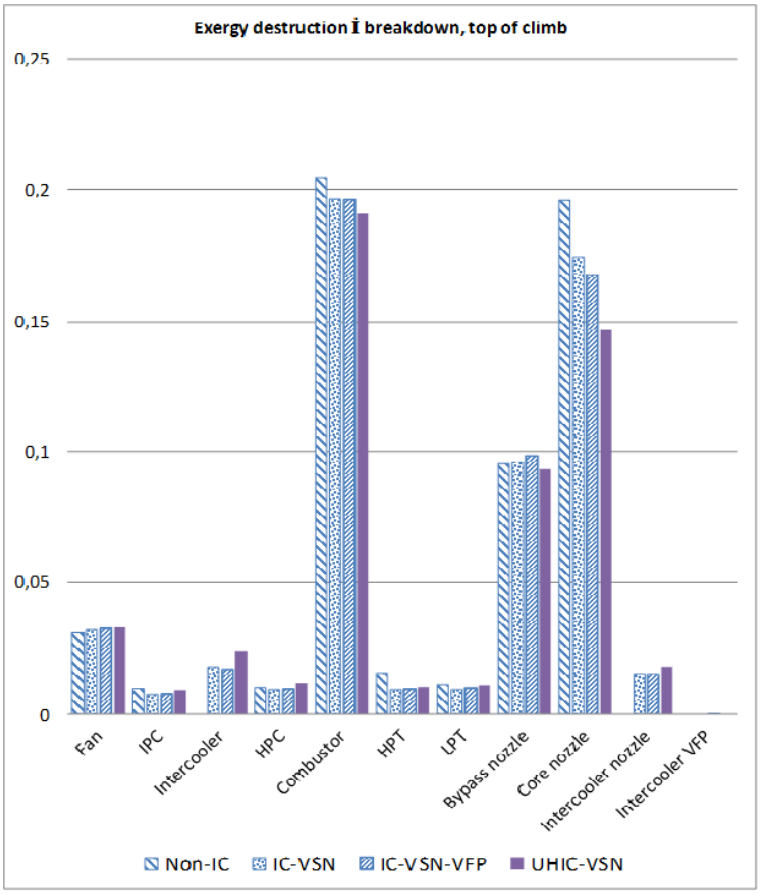

Figure 3.8.4: *Engine components exergy destruction per unit time, top-of-climb point*

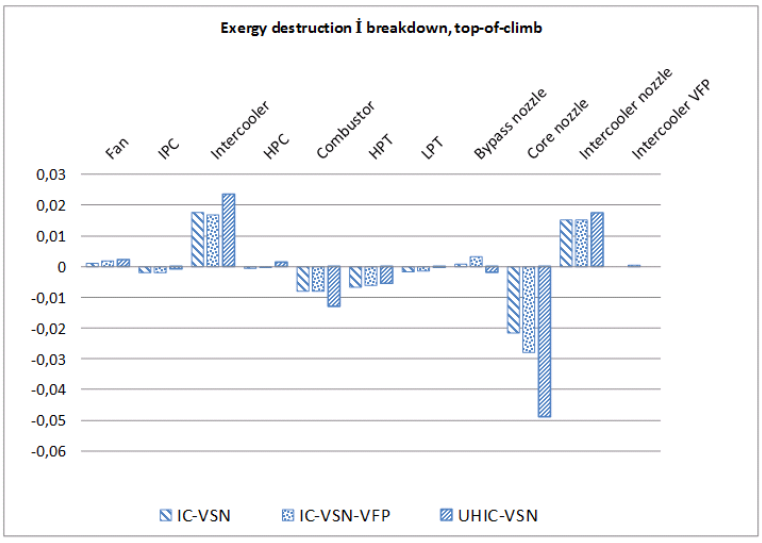

Figure 3.8.5: *Engine components exergy destruction per unit time subtract reference data, top-of-climb point*

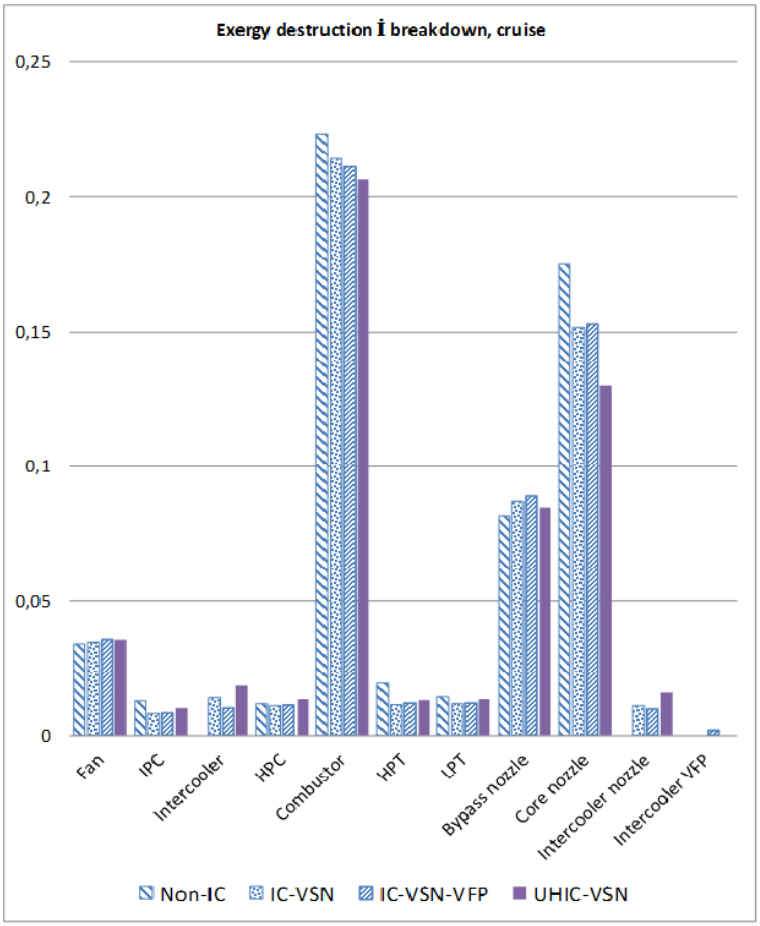

Figure 3.8.6: *Engine components exergy destruction per unit time, cruise point*

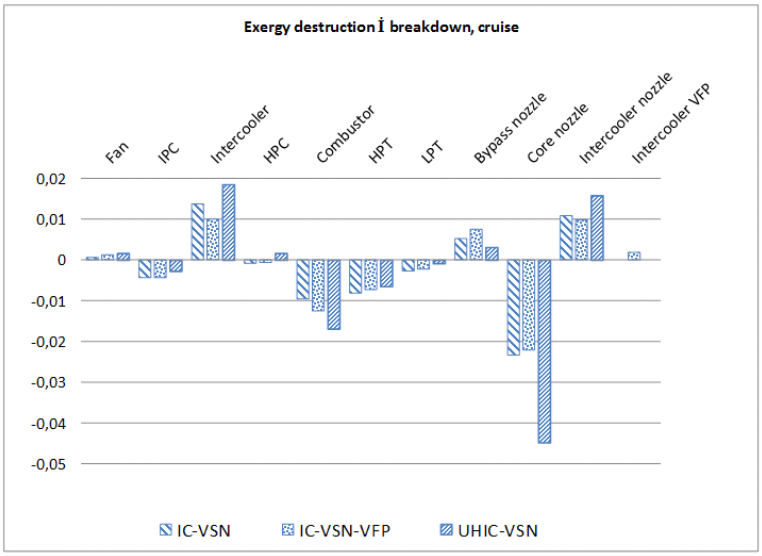

Figure 3.8.7: *Engine components exergy destruction per unit time subtract reference data, cruise point*

3.9 Emission consideration

Aero engines produce emissions like other fossil fuel combusting machines. For the two most important emissions, CO_2 and NO_x, simplified estimations can be made. As the carbon dioxide emissions are basically proportional to the fuel consumption level, the amount of reduction in the carbon dioxide emissions will be the same as the fuel burn reduction. The NO_x emissions are assessed by calculating the NOx severity parameter, S_{NOx}, as defined in [50, 51]:

$$S_{NOx} = (\frac{p_3}{2964.5kPa})^{0.4} \cdot e^{(\frac{T_3 - 826.26K}{194.39K} + \frac{6.29 - war * 100}{53.2})} \tag{3.9.1}$$

where the 'war' stands for water-air-ratio. T_3 and p_3 are the pressure and temperature at the entry of the combustor. Here, in this assessment, the air is assumed to be dry. Together with the consideration of SFC reduction, the NO_x emission during the mission can be corrected.

In Paper D, it has been concluded that intercooling could reduce NO_x effectively, through the comparison between the two intercooled engines with take-off OPR 79 and the non-intercooled engine, especially during take-off. On the other hand, due to the increase in the temperature and pressure at the entry of the combustor when the VSN and VFP kicks in at high altitude operation, the severity of the NO_x parameter increases. However, it is believed that the intercooling control through the VSN and VFP is necessary to keep the intercooler incurred losses down. Therefore a balance consideration has to be made between the fuel burn, CO_2 and NO_x for the intercooled engines studied in this thesis.

Unfortunately, the ultra-high OPR intercooled engine, which has a doubled pressure and similar temperature to the inlet of the combustor compared to the non-intercooled engine, shows a large increase in NO_x for all the operating points.

4 Aero engine intercooler experimental validation

In order to validate the intercooler conceptual design presented in Chapter 2, experimental work using PIV and pressure measurements was performed. The main objective is to firstly confirm the aerodynamic performance of the intercooler ducts, at the same time validate the porous media model and CFD tool through the comparison between the experiment results and CFD. Aiming at a Technology Readiness Level 3 (TRL3) - analytical and experimental critical function and/or characteristic proof of concept, following goals are set:

1. **Flow development within the inflow duct.** In previous work done on the intercooler design, see Paper B, it has been shown that the inflow duct introduces about 35% of the total loss incurred in the intercooler. This number could be even higher without the vane used to reduce the risk for flow separation in the inflow duct. Furthermore, the pressure distribution developed in the inflow duct and particularly in the inflow guide vane region strongly influences the flow distribution in the downstream heat exchanger tube stack. For this reason, pressure measurements were fitted at the bottom of the inflow duct to verify the flow development within the inflow duct.

2. **Flow topology within the crossover duct.** Previous experimental work on aero engine heat exchangers has mostly been performed in the region relatively far downstream of the heat transfer matrices where the flow is fully developed. By visualizing the flow field close to the tube stacks, the differences between the porous media modeling and the real flow can better be understood, in particular for this tubular type intercooler.

3. **Flow distribution within the tube stacks.** A key intercooler design criteria is to obtain an evenly distributed flow in the tube stacks. This gives the lowest average velocity in the tubes and hence the lowest pressure loss for the required heat transfer. The flow distribution within the heat exchange tube stacks can experimentally be verified through individual tube velocity measurements.

4. **Overall pressure losses.** The outlet total pressure profile of the intercooler system should be included to confirm the overall performance of the intercooler.

4.1 Intercooler Manufacture

To be able to perform PIV measurements is the primary requirement of the test rig and hence the optical access is a priority. Together with the difficulty of manufacturing the complex shape of the ducts and the relatively large number of flat tubes, rapid prototyping stereolithography (SLA) was selected as it could achieve a high accuracy and a good surface finish for high detail and thin walls. The 3D printing company ACRON, Sweden, was chosen as the manufacturer. With an optically clear and near colorless material, WaterShed-XC11122, it was believed that the 3D printed transparent parts could be applied to support the PIV measurements. However, there were three iterations have been performed for the heat exchanger manufacturing.

The first iteration on the intercooler manufacturing included the implementation of the heat exchanger CAD models which were transferred to the manufacturer to assess the cost and to make a test print. The test print of the tube bundle showed some problems on the 3D printing (SLA) of the bent elliptical tubes, such as blockage inside tubes, insufficient tube surfaces finish and insufficient tube stiffness. These deficiencies can be seen from Figure 4.1.1. Therefore, a second iteration on the rig design was performed and decision has been made to change the bent tube concept into a straight type to avoid the insufficient tube surfaces finish and to improve the stiffness without additional mechanical supports. The elliptical tube aspect ratio has been reduced from 8 to 7 to avoid the blockage inside tubes. Each elliptical tube was decided to have a major axis length of 20.5 mm, a minor axis length of 3 mm and a tube thickness of 0.5 mm. In total there is 119 staggered tubes for one tube stack.

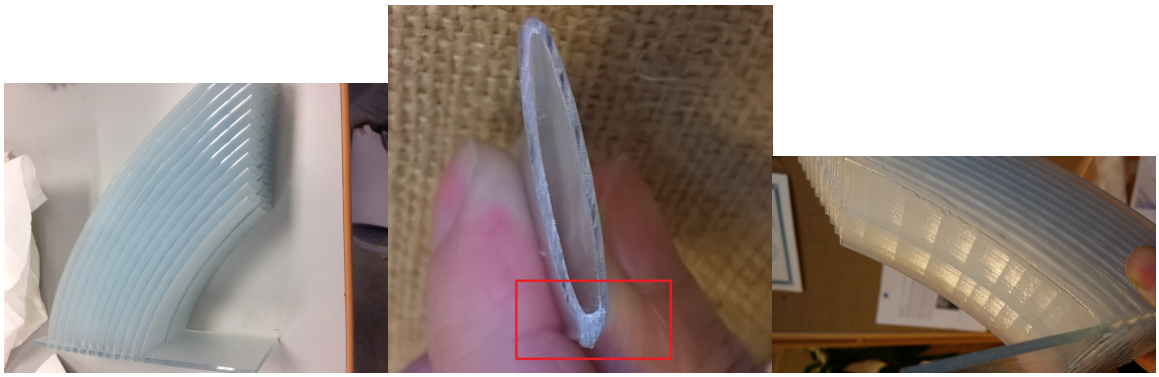

(a) (b) (c)

Figure 4.1.1: *Deficiencies of the bent elliptical tube stack test print*

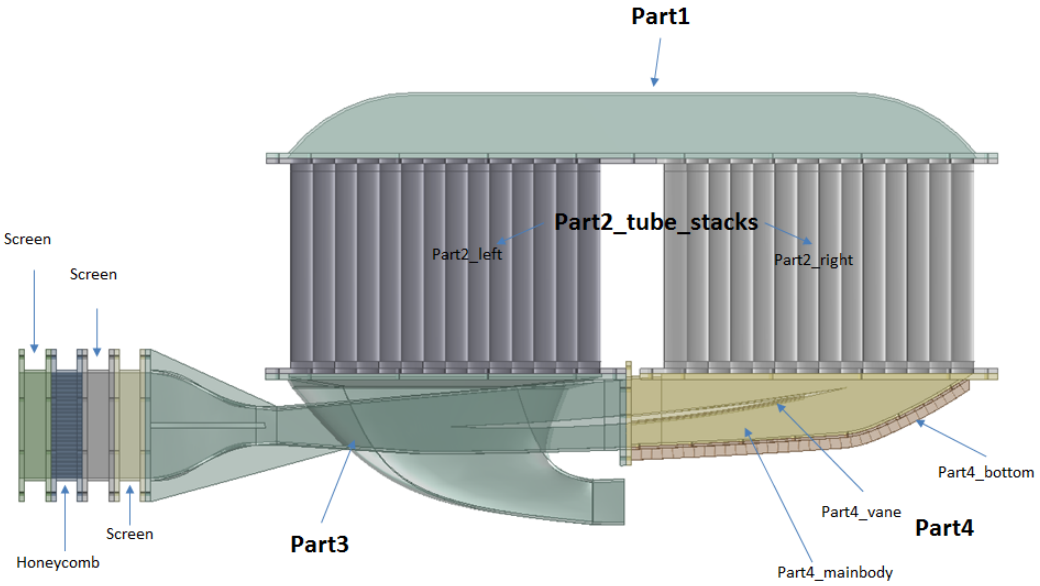

Figure 4.1.2: *Overview of the heat exchanger prototype model*

The intercooler prototype model, as shown in Figure 4.1.2, was manufactured part by part using SLA and is a half scale of its designed size. In order to get a uniform flow at the inlet of the intercooler, a settling chamber and a contraction section were added. The shape of the contraction was created with a Bell Mehta 5th order polynomial [52]. Note that the part3 was manufactured with the contraction duct as shown in Figure 4.1.2. Four pieces of the settling chamber including one honeycomb section with a mesh size of 1x1 m^2 and three screens were also 3D printed. Building the intercooler system in separate pieces makes it possible to generate a relatively large test object due to the limitation of the SLA machine (500 mm x 500 mm x 650 mm).

The second iteration was the first prototype fully formed by WaterShed-XC11122 using SLA which failed to achieve the sufficient optical performance for the PIV measurement in the crossover duct. With a duct wall thickness of 2.5 mm, optical distortions and a significant smearing of the particle images in the vertical direction were observed through the side walls of the crossover duct. The upper wall of the duct was less rough due to the peculiarities of SLA 3D prototyping with layer-by-layer upward extension of a manufacturing object. This means that upper wall did not distort the scattering light from tracer droplets very much. A modification of the crossover duct was hence done by replacing the two sides with Plexiglas to enhance the PIV performance, which

is the third iteration of the intercooler manufacturing. The PIV results of both the second and third iterations will be shown later. The comparison of the two crossover ducts is shown in Figure 4.1.3. The assembly of the intercooler prototype is shown in Figure 4.1.4.

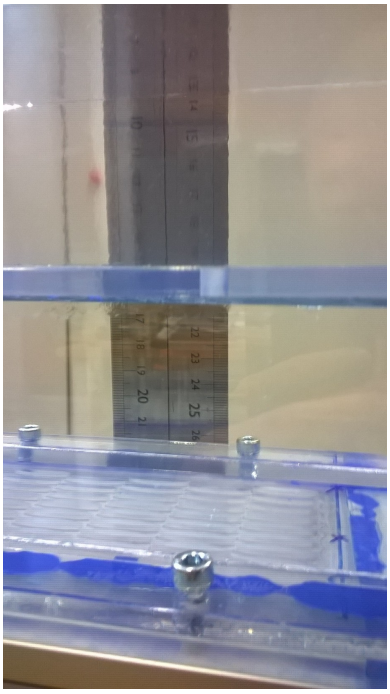

Figure 4.1.3: *Side wall view of the two crossover ducts. Up: Material WaterShed-XC11122; Down: Replacement by Plexiglas*

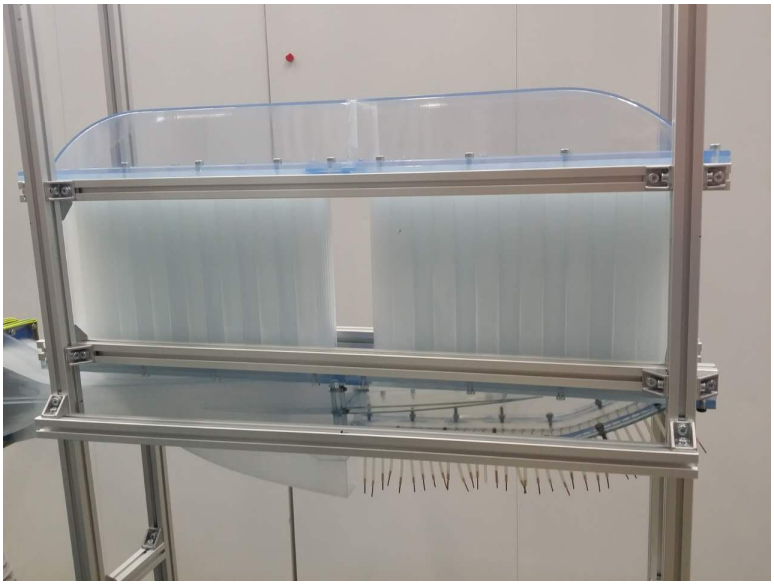

Figure 4.1.4: *Intercooler prototype assembly*

4.2 Rig design

Swegon FAHB-010 radial fan was selected as the flow charger and the performance curve of this fan is presented in Figure 4.2.1. To avoid vibration transmission from the fan, an aluminum-coated fiberglass coupling sleeve was used between the fan and the downstream components.

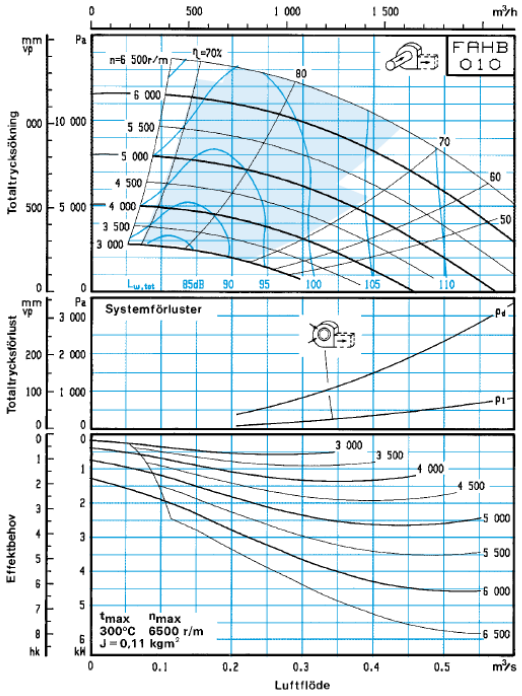

Figure 4.2.1: *Swegon FAHB-010 radial fan performance curve*

Three sets of measurements were performed in this study as described below.

1. As shown in the full setup demonstration of Figure 4.2.2, pressure measurements were performed at the mid plane of the rear bottom part of the inflow duct (part4) with 33 pressure measurement tabs, and at the outlet of the outflow duct with a Pitot tube. The pressure tabs are all in a size of 0.5 mm and evenly distributed as shown in Figure 4.2.3, the first pressure hole is located at the same axial position as the mid-point of the crossover duct.

2. A case with only the inflow duct and the inflow tube stack, illustrated in Figure 4.2.4, was performed to investigate the flow distribution through the tube stack. Since the access to the tubes can be very difficult with all the ducts installed, a separate test with only the inflow duct and one tube stack of the intercooler system has been performed. This allowed the flow distribution to be measured for the tubes by measuring the velocity at the center of each tube, see Figure 4.2.5.

3. PIV recorded the flow field on the four planes which cut through the crossover as shown in Figure 4.2.6, one horizontal plane at the mid position and three vertical planes with 15 mm distance between them. This was performed based on the full setup of the rig.

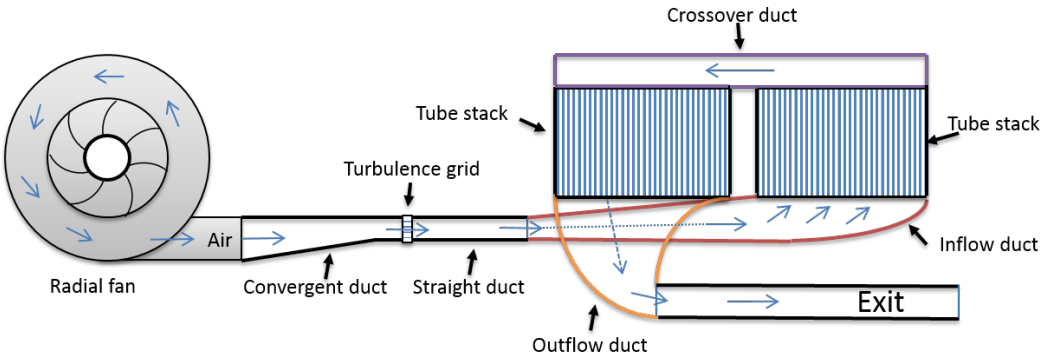

Figure 4.2.2: *Test rig full setup*

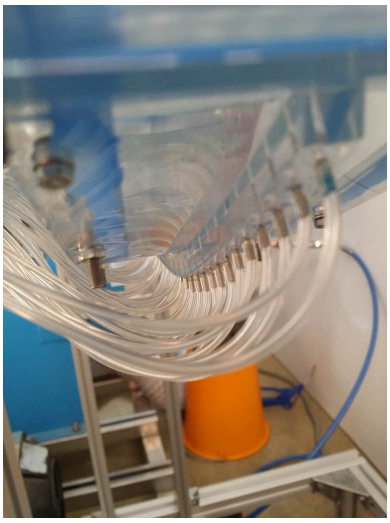

Figure 4.2.3: *Pressure tabs mountings*

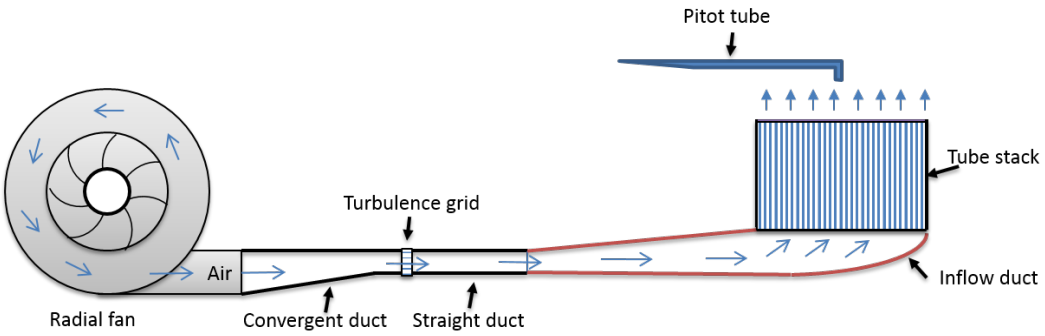

Figure 4.2.4: *Test rig of flow distribution case*

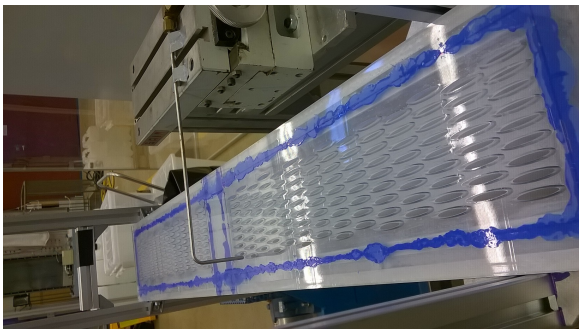

Figure 4.2.5: *Open tube stack view*

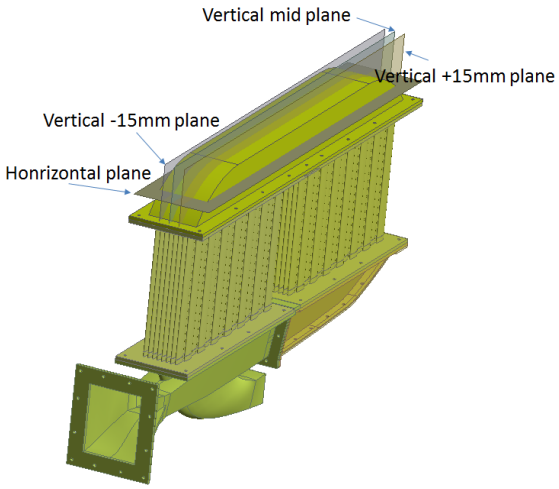

Figure 4.2.6: *Four planes cutting through crossover duct for PIV*

4.3 PIV setup

For PIV measurements, LaVision FlowMaster system was used. It consisted from a CCD camera LaVision Imager Pro x 4M, 2048x2048 pixel, with 7.4 um pixel size and a pulsed Nd:YAG double-cavity laser (Quantel EverGreen EVG00200) with 200 mJ energy per each pulse and pulse duration 10 ns. The camera was equipped with SIGMA AF 105 mm f/2.8 EX DG MACRO lens with f-number being set to 5.6. The optical configuration gave us a measurement area 97x97 mm and 72x72 mm for vertical and horizontal planes along the crossover duct with the magnification factors 0.16 and 0.22 correspondingly. Flow seeding was organized with an in-house atomizer device described in [53]. Water-glycol mixture SWEFOG Neutral-Pro HD Smoke Fluid was utilized in the atomizer. Aerosol was supplied directly to the inlet of the radial fan. The exhaust of the aerosol was organized outside the laboratory with a flexible pipe.

DaVis 8.2 (LaVision GmbH) was used for recording and processing PIV images. In total 7 and 9 measurement areas with 200 image pair in vertical and horizontal planes of the crossover duct were recorded. Sequential particle image pairs were acquired with the maximum frame rate for the camera in the double frame mode at 7.26 Hz. Particle image seeding density was 0.03 particles per square pixel area. The time separation between two successive laser pulses was set to 30 us. It allowed us to use final PIV interrogation areas with the size 32x32 px and 48x48 px, which leads to the in-plane spatial resolution for one velocity vector 1.5x1.5 mm and 1.7x1.7 mm for the vertical and horizontal planes. The reason for larger PIV interrogation areas in case of the horizontal plane despite the higher optical magnification was due to a bright background with the opaque tube bundles that scattered light and decreased the signal-to-noise ratio.

The laser sheet thickness was approximately 1.5 mm, which defined the spatial resolution in the out-of-plane direction. Four iterations of a multi-grid, multi-pass correlation algorithm from LaVision software was used to get instantaneous velocity fields starting from the size of the interrogation area equal to 64x64 px and 96x96 px. Before the correlation analysis the raw particle images were preprocessed by a subtracting sliding background intensity. The resultant mean velocity distributions were acquired by averaging 200 instantaneous velocity fields for all zones and stitching them together according to a reference scale that was recorded at the same time with the tracer particles. A full setup of the PIV measurements with the intercooler test-rig is presented in Figure 4.3.1.

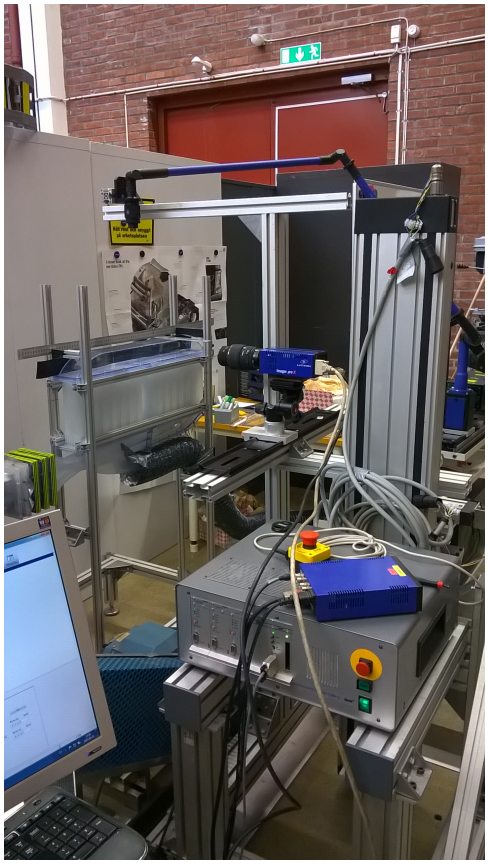

Figure 4.3.1: *Test rig with full PIV setup*

4.4 Comparison with CFD assessment

CFD simulations were performed with the same intercooler size and boundary conditions as in the test rig. Detailed settings are identical to the CFD simulations described in Chapter 2. The Reynolds number in the tubes based on the average velocity is around 3300 in this study. The surface roughness of the wall is obtained through measurement of one example piece of the 3D printed model by the Chalmers surface geometry group. A mass flow of 0.085 kg/s gives an inlet velocity in the contraction duct of 8.7 m/s, an outlet velocity of the intercooler 60 m/s and the highest velocity in the intercooler around 120 m/s. The comparison between the experiments with the CFD simulations is concluded below. Basically, the CFD results shown a good agreement with the experiments.

4.4.1 Inflow duct

As shown in Figure 4.4.1, by normalizing the pressure to the reference pressure, the pressure distribution at the bottom of the inflow duct predicted by CFD shows a similar trend as the experimental data with a maximum difference of 0.4%.

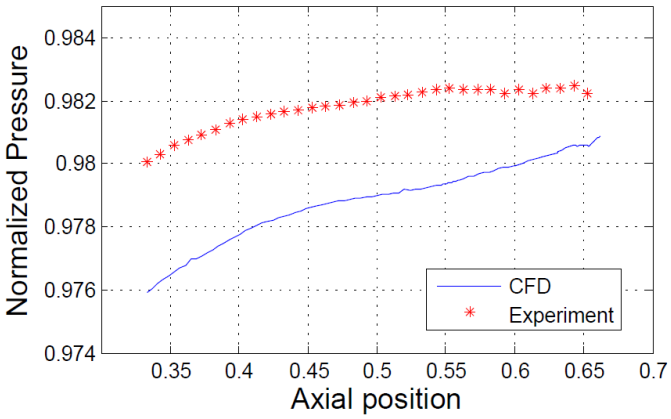

Figure 4.4.1: *Pressure distribution at the bottom of the inflow duct rear part (part4)*

4.4.2 Outflow duct

The contours of the total pressure at the intercooler outlet in Figure 4.4.2 shows the comparison between the experiment and the CFD prediction. The magnitude is normalized by the average total pressure at the inlet of the intercooler. As can be expected the contours present good agreement with each other, which supports the capability of the porous media model for well describing the macroscopic behavior of the intercooler matrices.

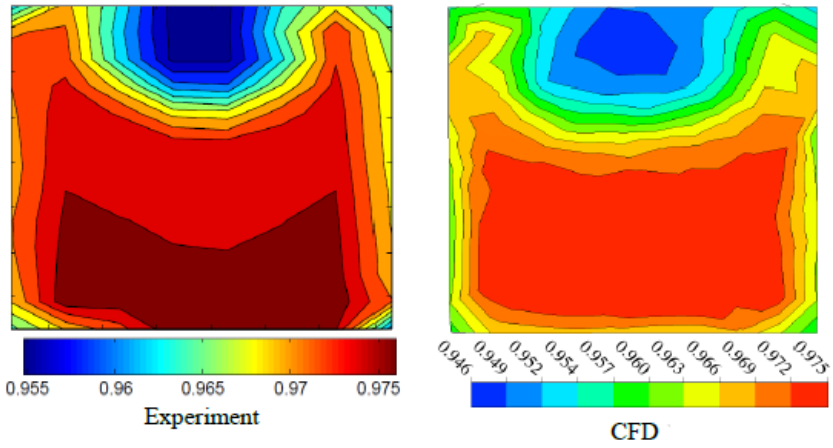

Figure 4.4.2: *Comparison of the total pressure plot at the outlet of the intercooler, Experimental result (left) and CFD result (right)*

However, both the numerical and experimental results show a recirculation region at the outlet plane which is because of the aggressive C turn of the outflow duct as can be seen in the intercooler sketch. CFD over-predicts the loss in the recirculation region with around 1% as can be read from the color bar. The flow quality entering the HPC is quite important in order to avoid reducing surge margin as well as preventing high cycle fatigue. In a nonintercooled engine the upstream compressor would have to show a continuously reducing radius in the last few compressor stages in order to match the curvature of the duct between the exit and the HPC entrance. Having a downstream intercooler it would be more obvious to use a constant tip design upstream of the intercooler to lift the upstream interface, see Figure 4.4.3. This would allow a less aggressive curvature in the intercooler outflow duct and a substantially reduced separated flow area. A new design with a higher IPC installation (2 cm) was hence performed with CFD since the capability of simulation based design has been confirmed by the experiment. The result of the new design is given in Figure 4.4.4, in which a relatively well-distributed flow is observed.

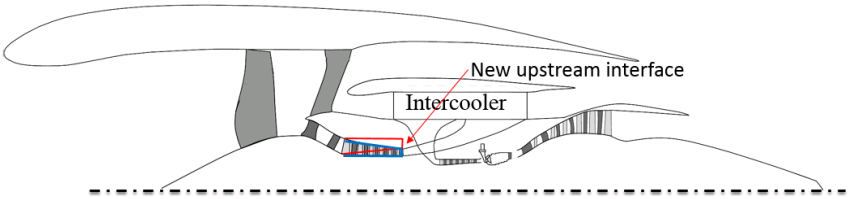

Figure 4.4.3: *Higher radius IPC installation illustration*

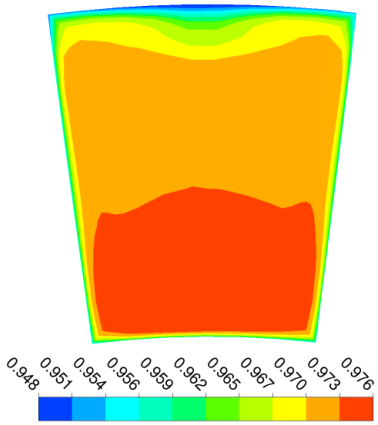

Figure 4.4.4: *Total pressure plot at the outlet of the intercooler, CFD result with a higher radius IPC installation*

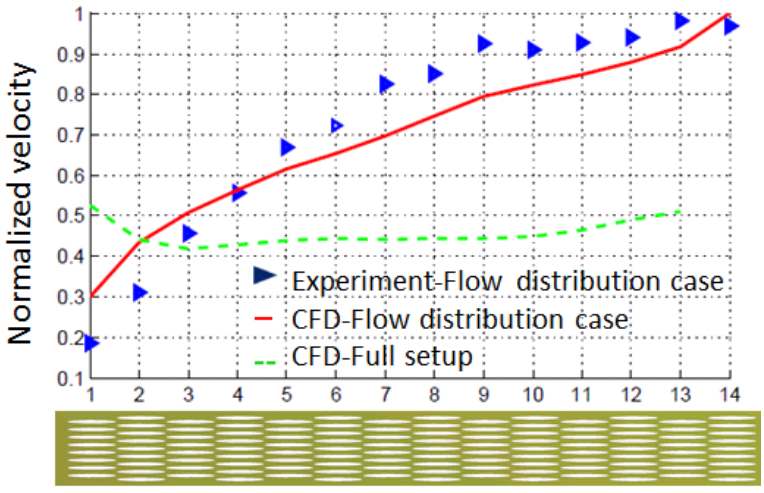

Figure 4.4.5: *Normalized average flow velocity for each tube column of the inflow tube stack*

4.4.3 Flow distribution within tube stack

In Figure 4.4.5, the average flow velocity for each tube column is given as normalized by the maximum velocity through the tubes, where the CFD result gives good prediction compared with the experimental work. It should be noticed that the velocity curve for the flow distribution case is quite similar to the pressure distribution curve in the inflow duct. On the other hand, with the crossover duct mounted, see the green dash line in Figure 4.4.5, the averaged velocity curve is relatively flat showing a good flow distribution across the inflow tube stack.

4.4.4 Crossover duct

With the visualization of the flow field, a clearer picture of the capability of the porous media model could be obtained. As shown in Figure 4.4.6, Figure 4.4.7 and Figure 4.4.8, the finger shaped flow pattern at the right corner of the PIV record shows the largest difference from the CFD contour. Because of the nature of the staggered real tubes, the flow ejecting from the tubes is discrete while in CFD the flow coming out from the porous media is continuous. However, after a short distance the flow beams start to mix, and then the flow pattern develops very similar to the case with the porous media model. As expected, separations from the upper wall can be observed on the left corner of the crossover duct because of the adverse pressure gradient. From plane to plane, the flow separation point on the left corner of the duct predicted by CFD matches the experimental results quite well. However, the flow in the crossover duct is asymmetric as the separation shown on the -15 mm plane is much larger than the other two planes.

The first round PIV measurements with the WaterShed XC11122 formed crossover duct can be also seen in these Figures. The quality of the result is quite bad compared with the second round PIV. As mentioned earlier the material WaterShed XC11122 does not have an optical performance as good as the Plexiglas. The record from the second round PIV also shows some incompleteness at the place close to the bottom of the figures. This is mainly because of that the two Plexiglas sides and the 3D printed structure are glued together and that the conjunction part introduces large optical distortion.

For the horizontal view recorded in this study, Figure 4.4.9, it can be seen that the velocity close to the wall is higher than the center of the flow region. In CFD, the under-predicted pressure at the mid of the bottom face in the inflow duct drives an even lower velocity in the center of the tube stack. Therefore, the velocity gradient from the wall to the flow center of the porous model is larger than that in the experiment as shown in Figure 4.4.9. This results in an early separation from the side wall in the CFD result.

4.4.5 Conclusion from the comparison

Through the comparison between the CFD results and experiment, the aerodynamic performance of the tubular intercooler system is given. The conceptual design of this intercooler using CFD is validated. Even though the detailed flow field records have highlighted the difference between a porous media model and a real geometry. The porous media model still shows a sufficiently realistic representation of the real geometry. The experimental results indicate that the CFD predictions are sufficiently accurate to confirm the critical design points, such as flow distribution within the heat transfer units and overall intercooler performance. To obtain a good conceptual intercooler design, resolving the flow inside the tube stacks seems less critical. With this capacity, the intercooler components can be simulated as a whole system to reveal the strong interaction between the components.

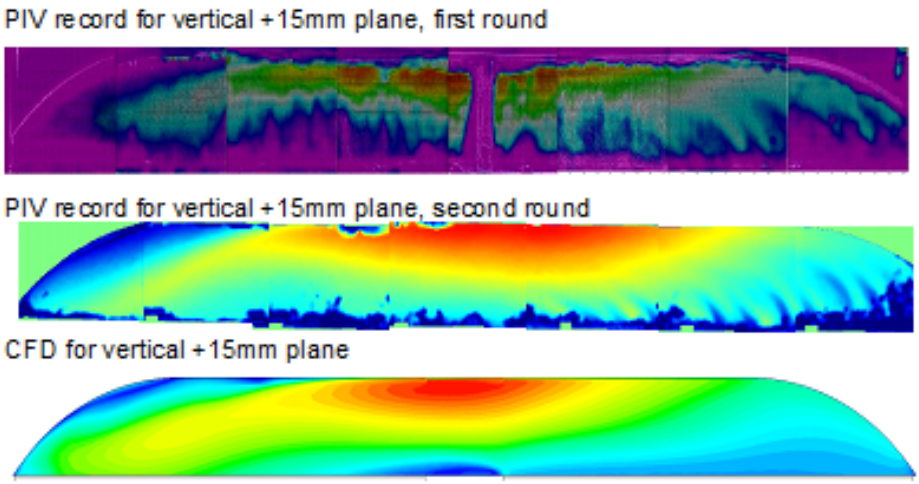

Figure 4.4.6: *PIV versus CFD on the +15 mm vertical plane of the crossover duct*

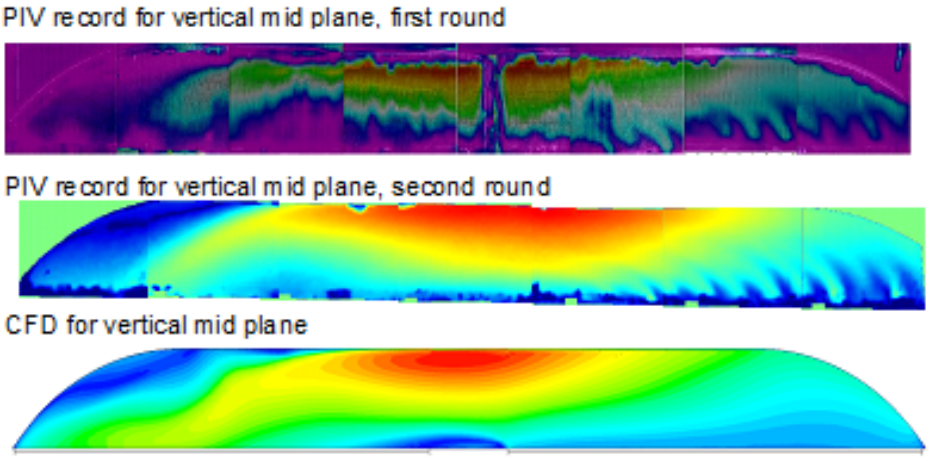

Figure 4.4.7: *PIV versus CFD on the mid vertical plane of the crossover duct*

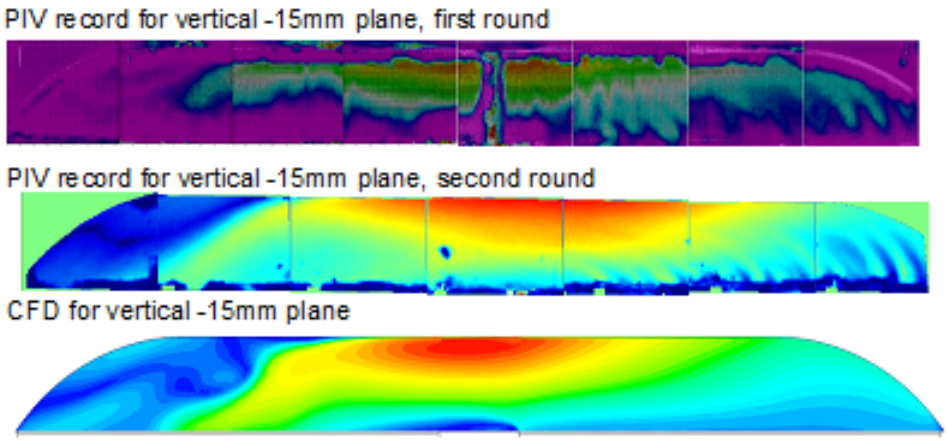

Figure 4.4.8: *PIV versus CFD on the -15 mm vertical plane of the crossover duct*

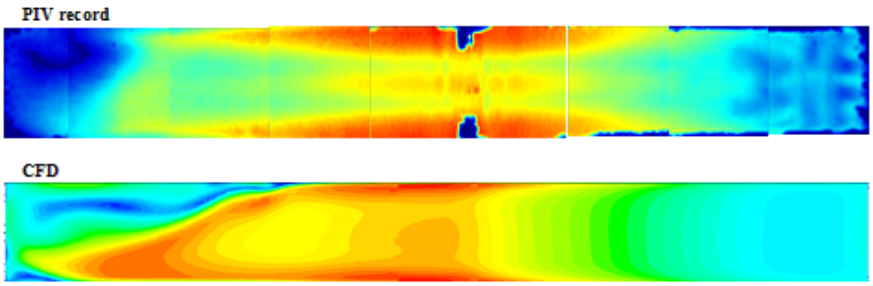

Figure 4.4.9: *PIV record (Up) and CFD result (Down) of the flow velocity at the horizontal plane of the crossover duct*

5 Papers Summary

This chapter briefly summarized the five appended papers (Papers A-E) and specifies the author's contribution to all the papers.

5.1 Paper A: Assessment of The Performance Potential for a Two-pass Cross Flow Intercooler for Aero Engine Applications

My contribution for this conference paper, besides being the lead author, was to carry out the engine performance simulations and analysis as well as write the draft of the paper. Professor Tomas Grönstedt supervised the work and provided support to the simulation, the analysis and the writing of the paper. Dr. Konstantinos Kyprianidis reviewed the work and provided support to the analysis and the discussion.

The aim of this paper is to estimate the performance potential of the two-pass cross flow intercooler presented in this thesis. Two geared turbofans are established in this paper, one is intercooled with the presented intercooler and another one is non-intercooled. Through the comparison between the two engines for the same long range mission, a reduction of 4.8% fuel burn is obtained by intercooling. Benefits are mainly derived from the higher OPR of the intercooled geared turbofan and the control of the intercooling at different operating points. In general, the two-pass cross flow intercooler is viewed to give a relatively small internal pressure loss and a relatively high external pressure loss. The transferred heat with this intercooler concept is relatively modest. However, the modest heat transfer is sufficient to enable the higher OPR for a better efficiency while the relatively large external pressure loss could be limited by the use of a variable separate nozzle.

In this paper, because of fill-in-error some data in Table 4 is different from the correct parameters provided in this thesis.

5.2 Paper B: Conceptual Design of a Two-Pass Cross Flow Aero-Engine Intercooler

My contribution for this journal paper, besides being the lead author, was to perform the CFD simulations and establish the correlations, as well as write the draft of the paper. The co-author supervised the work and provided support to the analysis and writing.

In this paper, the aerodynamic design of the intercooler presented in this thesis is described. Porous media CFD simulations were carried out to improve the aerodynamic performance of the intercooler associated ducts and establish the ducts performance correlations. For the intercooler external side, five sets of tube arrangement were evaluated by 2D CFD. The results are discussed and the correlation of each is given.

5.3 Paper C: First and Second Law Analysis of Intercooled Turbofan Engine

My contribution for this journal paper, besides being the lead author, was to perform the engine performance simulations and exergy analysis, as well as write the draft of the paper. Professor Tomas Grönstedt supervised the work and provided support to the engine performance analysis, exergy analysis and writing. Oskar Thulin provided support to the exergy analysis and wrote the exergy theory part.

In this paper, an ultra-high OPR intercooled geared engine with an axial-radial HPC design is firstly described. With the last two stages of the HPC replaced by a radial compressor, the last blade height limit induced by the

excessive OPR is eliminated. A maximum OPR of 140 was obtained at TOC for this engine. By comparing it with a non-intercooled geared engine and an pre-studied intercooled engine, a net fuel burn reduction of 5.3% and 0.8% is observed respectively. Besides the traditional performance study, analysis is also conducted using an exergy breakdown, i.e. quantifying the losses into a common currency by applying a combined use of the first and second law of thermodynamics. It is believed that the exergy analysis tends to provide a clear quantitative picture of the important effects, whereas the traditional performance data provides the details necessary for the interpretation.

5.4 Paper D: Aero Engine Intercooling Optimization Using A Variable Flow Path

My contribution for this conference paper, besides being the lead author, was to carry out the engine performance simulations and analysis, engine emissions estimation as well as write the draft of the paper. The co-author supervised the work and provided support to the analysis and writing.

The aim of this paper is to further optimize the intercooled geared engine established in Paper A by introducing a variable flow path at the internal side of the intercooler. As mentioned in Paper A, a variable separate nozzle has been used to limit the loss of the intercooler external side at cruise. The loss incurred in the intercooler internal hot side remains at a considerably high level. A variable flow path concept is used to bypass half of the intercooler internal hot flow from the intercooler at cruise. It leads to a further reduction of 0.5% cruise SFC and result in a total of 4.9% fuel burn reduction compared with an optimized advanced geared engine. The benefit is obtained through the loss reduction of the intercooler internal side.

5.5 Paper E: Experimental Validation of The Aerodynamic Performance of An Aero Engine Intercooler

My contribution for this journal paper, besides being the lead author, was to build the test rig, perform the measurements, establish the CFD simulations as well as write the draft of the paper. Professor Tomas Grönstedt supervised the work, provided support to the analysis, the discussions and the writing of the paper. Dr. Mikhail Tokarev performed the PIV measurements and provided the description of the PIV setup. Erwin Adi Hartono supported the establishment of the test rig and provided guidance to the measurements. Associated Professor Valery Chernoray provided support to the experimental work.

The aim of this paper is to validate both the aerodynamic performance of the aero engine intercooler studied in this thesis as well as the CFD design tool. With the help of rapid prototyping stereolithography, the intercooler was manufactured with high accuracy and good surface finish. The experiments were performed mainly by PIV and pressure measurements. Generally, comparing the results of the CFD results and the experiment results, good agreement was obtained. By comparing the pressure data inside of the inflow duct, the flow distribution within the intercooler tube stack, the detailed flow topology inside of the crossover duct and the intercooler outlet flow profile, it has been confirmed that the porous media model has the capability of establishing a sufficiently realistic representation of the real geometry. Furthermore, a relatively uniform flow distribution has been observed within the intercooler tube stack.

5.6 Other related publications

5.6.1 Concept Description and Assessment of the Main Features of A Geared Intercooled Reversed Flow Core Engine

My contribution for this journal paper, as one of the co-authors, was to provide the correlations of the intercooler system which was used to perform the engine performance study in this paper.

This paper is not included in this thesis.

5.6.2 An Outlook for Radical Aero Engine Intercooler Concepts

My contribution for this conference paper, as one of the co-authors, was to provide the fuel heat rejection section, both the analysis and writing.

This paper is not included in this thesis.

6 Concluding remarks

This thesis focuses on establishing a systematic understanding of the intercooled turbofan concept. The core is the conceptual design and experimental validation for the key component of aero engine intercooling. By integrating a validated intercooler system module into the aero engine system, a reliable behaviour of the intercooled core engine components are simulated.

Generally, a lower fuel burn and lower emissions could be obtained with aero engine intercooling because of a number of benefits resulting from a lower HPC inlet temperature. With a combined use of traditional performance and exergy breakdown analysis, the benefits of the optimal engines evaluated in this thesis can be listed in the following rank: a higher thermal efficiency for an increased OPR, a smaller core, a less HPT cooling flow need and a less HPC compression power requirement.

The key component of an intercooled turbofan, the intercooler, must be highly efficient, compact and light to gain the benefits of intercooling. To reduce the size and weight is the first priority as the other drawbacks like losses and heat rejection from the core can be largely limited by the associated intercooling control.

Intercooling control, as a way of limiting the associated losses incurred by the intercooler system, has its drawbacks. Firstly, a reduction of intercooling could increase the NO_x emissions because of the high pressure and high temperature nature of an intercooled engine. Secondly, reducing the amount of intercooling by closing the separate nozzle would lead to a decrease in the fan mass flow and an increase in the jet velocity. This results in a decreased propulsive efficiency and pushes the fan operating point closer to the surge margin. Thirdly, the effect of the temperature distortion resulted from the VFP concept needs to be figured out.

Considerations must be taken to the other engine components which can be affected negatively by the intercooling associated changes in the engine. In particular the HPC, the last blade height of which is a critical parameter for its efficiency. An axial-radial concept is investigated as a way of eliminating this side-effect. LPT cooling should be added since the LPT inlet temperatures of the engines are above what can be run with uncooled blades.

As a convenient approach of developing heat exchanger for various applications, porous media CFD is confirmed capable of setting up a sufficiently realistic intercooler design method. However, the difference between a porous media model and a real geometry is also highlighted. If this discrepancy is important for the design of the application a more advanced flow simulation or experimental work is needed. The current technology readiness level of the work is TRL 3.

Bibliography

[1] AIRBUS S.A.S. Future Journeys 2015-2034, Global Market Forecast.

[2] R. Avellan. *On The Design of Energy Efficient Aero Engines: Some Recent Innovations*. PhD Thesis, Chalmers University of Technology, Gothernburg, Sweden, 2011.

[3] Grace's Guide To British Industrial History. $http://www.gracesguide.co.uk/Rolls-Royce:RM60$.

[4] A. Lundbladh and A Sjunnesson. Heat Exchanger Weight and Efficiency Impact on Jet Engine Transport Applications. *The 16th International Symposium on Air Breathing Engines, Cleveland, Ohio, ISABE-2003-1122*, Sep. 2003.

[5] K. Kyprianidis, A. Rolt, and T. Grönstedt. Multidisciplinary Analysis of a Geared Fan Intercooled Core Aero-Engine. *Journal of Engineering for Gas Turbines and Power*, 136(1), Oct. 2013.

[6] W. M. Kays and A. L. London. *Compact Heat Exchanger, 2nd ed.* McGraw-Hill, ISBN 07-033391-2, 1964.

[7] A. Rolt, N.J. Baker, and Rolls-Royce plc. Intercooled Turbofan Engine Design and Technology Research in the EU Framework 6 NEWAC Programme. *ISABE-2009-1278*, 2009.

[8] G. Wilfert, J. Sieber, A. Rolt, N. Baker, A. Touyeras, and S Colantouni. New Enviromentally Friendly Aero Engine Core Concepts. *The 18th International Symposium on Air Breathing Engines, Beijing, China, ISABE-2007-1120*, Sep. 2007.

[9] P. W. Kwan, D. R. H. Gillespie, R. D. Stieger, and A. M. Rolt. Minimising Loss in a Heat Exchanger Installation for an Intercooled Trubofan Engine. *Proceedings of ASME Turbo Expo 2011, GT2011-45814*, June 6-10 2011.

[10] C. A. Barrow, J. F. Carrotte, A. D. Walker, and A. M. Rolt. Aerodynamic Performance of a Coolant Flow Off-Take Downstream of an OGV. *Proceedings of ASME Turbo Expo 2011, GT2011-45888*, June 6-10 2011.

[11] A. D. Walker, J. F. Carrotte, and A. M. Rolt. Duct Aerodynamics for Intercooled Aero Gas Turbines: Constraints, Concepts and Design Methodology. *Proceedings of ASME Turbo Expo 2009: Power for Land, Sea and Air, GT2009-59612*, June 8-12 2009.

[12] A. D. Walker, G. S. Regunath, J. F. Carrotte, and P. A. Denman. Intercooled Aero-Gas-Turbine Duct Aerodynamics: Core Air Delivery Ducts. *Journal of Propulsion and Power*, 28(6), Nov.-Dec. 2012.

[13] NEWAC official website. $http://www.newac.eu$.

[14] Bruner, S., Baber, S., Harris, C., Caldwell, N., Keding, P., Rahrig, K., Pho, L., and Wlezian, R. NASA N+3 Subsonic Fixed Wing Silent Efficient Low-Emissions Commercial Transport (SELECT) Vehicle Study . Technical report, NASA, NASA/CR-2010-216798, 2010.

[15] Y. Ito and T. Nagasaki. Suggestion of Intercooled and Recuperated Jet Engine Using Already Equipped Components as Heat Exchangers. *The 47th AIAA/ASME/SAE/ASEE Joint Propulsion Conference and Exhibit*, pages AIAA 2011–6102, 2011.

[16] Y. Ito, N. Inokura, and T. Nagasaki. Conjugate Heat Transfer in Air-to-Refrigerant Airfoil Heat Exchangers. *Journal of Heat Transfer, ASME*, page DOI: 10.1115/1.4027554, 2014.

[17] L. Xu. *Analysis and Evaluation of Innovative Aero Engine Core Concepts*. PhD Thesis, Chalmers University of Technology, Gothernburg, Sweden, 2011.

[18] L. Xu and T Grönstedt. Design and Analysis of an Intercooled Turbofan Engine. *Journal of Engineering for Gas Turbines and Power*, 132, Nov. 2009.

[19] Xin Zhao and Tomas Grönstedt. Conceptual design of a two-pass cross-flow aeroengine intercooler. *Proceedings of the Institution of Mechanical Engineers, Part G: Journal of Aerospace Engineering*, page 0954410014563587, 2014.

[20] W. A. Khan, J. R. Culham, and M. M. Yovanovich. Fluid Flow Around and Heat Transfer from Elliptical Cylinders. *Journal of Thermophysics and Heat Transfer*, 19(2), April-June 2005.

[21] H. Grieb and W. Schlosser. Shaped Tube with Elliptical Cross-section for Tubular Heat Exchangers and a Method for Their Manufacture. *United States Patent*, (4766953), August 1988.

[22] M. J. Marongiu. Compressibility Effects in the Design of Gas-cooled Microchannel Heat Sinks. *InterSociety Conference on Thermal Phenomena*, 1996.

[23] X. Zhao, T. Grönstedt, and K. Kyprianidis. Assessment of The Performance Potential for a Two-pass Cross Flow Intercooler for Aero Engine Applications. *The 21st ISABE conference, September 9-13, Busan, South Korea*, 2013.

[24] ANSYS Ltd. *Ansys 14.0 Help*. ANSYS Ltd., release 14.0 edition, 2011.

[25] ANSYS Ltd. CFX. On the WWW. URL verb+http://www.ansys.com.

[26] ANSYS Inc. Innovative Turbulence Modeling: SST Model in ANSYS CFX. Technical report, ANSYS Inc., Canonsburg, PA, 2006.

[27] F. Menter, J.C. Ferreira, T. Esch, and B. Konno. The SST Turbulence Model with Improved Wall Treatment for Heat Transfer Predictions in Gas Turbines. *Proceeding of the International Gas Turbine Congress, Tokyo*, Nov. 2003.

[28] K. Kritikos, C. Albanakis, D. Missirlis, Z. Vlahostergios, A. Goulas, and P. Storm. Investigation of the Thermal Efficiency of a Staggered Elliptic-tube Heat Exchanger for Aeroengine Applications. *Applied Thermal Engineering*, 30:134–142, 2010.

[29] D. Missirlis, S. Donnerhack, O. Seite, C. Albanakis, A. Sideridis, K. Yakinthos, and A. Goulas. Numerical Development of a Heat Transfer and Pressure Drop Porosity Model for a Heat Exchanger for Aeroengine Applications. *Applied Thermal Engineering*, 30:1341–1350, 2010.

[30] D. Missirlis, K. Yakinthos, A. Palikaras, K. Katheder, and A. Goulas. Experimental and Numerical Investigation of the Flow Field through a Heat Exchanger for Aeroengine Applications. *Int. J.Heat and Fluid Flow*, 26:440–458, 2005.

[31] K. Yakinthos, D. Missirlis, A. Palikaras, P. Storm, B. Simon, and A. Goulas. Optimization of the design of recuperative heat exchangers in the exhaust nozzle of an aero engine. *Appl Math Model*, 31(11):2524–2541, 2007.

[32] Mesbah G Khan and Amir Fartaj. A review on microchannel heat exchangers and potential applications. *International journal of energy research*, 35(7):553–582, 2011.

[33] S. E. Haaland. Simple and explicit formulas for the friction factor in turbulent pipe flow. *J. Fluids Eng.*, 105(1):89–90, 1983.

[34] V. Gnielinski. New equations for heat and mass transfer in turbulent pipe and channel flow. *International Chemical Engineering*, 16:359–368, 1976.

[35] T. Grönstedt. *Development of Methods for Analysis and Optimization of Complex Jet Engine Systems*. PhD Thesis, Chalmers University of Technology, Gothernburg, Sweden, 2000.

[36] E Onat and GW Klees. A method to estimate weight and dimensions of large and small gas turbine engines. 1979.

[37] Jean-Jacques Korsia and Guy De Spiegeleer. Vital, an european r&d program for greener aero-engines. In *25th Congress of International Council of the Aeronautical Sciences, Hamburg, Germany*, pages 2006–5, 2006.

[38] Günter Wilfert, Joerg Sieber, Andrew Rolt, Nick Baker, Armel Touyeras, and Salvatore Colantuoni. New environmental friendly aero engine core concepts. In *XVIII International Symposium of Air Breathing Engines, Beijing, China, Sept*, pages 2–7, 2007.

[39] Linda Larsson, Tomas Grönstedt, and Konstantinos G Kyprianidis. Conceptual design and mission analysis for a geared turbofan and an open rotor configuration. In *ASME 2011 Turbo Expo: Turbine Technical Conference and Exposition*, pages 359–370. American Society of Mechanical Engineers, 2011.

[40] Konstantinos Kyprianidis, A Dax, Stephen Ogaji, and Tomas Grönstedt. Low pressure system component advancements and its impact on future turbofan engine emissions. *Proceedings of the ISABE*, pages 7–11, 2009.

[41] William Camilleri, Eduardo Anselmi, Vishal Sethi, Panagiotis Laskaridis, Tomas Grönstedt, Xin Zhao, Andrew Rolt, and Pedro Cobas. Concept description and assessment of the main features of a geared intercooled reversed flow core engine. *Proceedings of the Institution of Mechanical Engineers, Part G: Journal of Aerospace Engineering*, page 0954410014557369, 2014.

[42] R. C. Wilcock, J. B. Young, and J. H. Horlock. The Effect of Turbine Blade Cooling on the Cycle Efficiency of Gas Turbine Power Cycles. *Journal of Engineering for Gas Turbines and Power*, 127, Jan 2005.

[43] Konstantinos G Kyprianidis and Andrew M Rolt. On the optimization of a geared fan intercooled core engine design. *Journal of Engineering for Gas Turbines and Power*, 137(4):041201, 2015.

[44] William Camilleri, Eduardo Anselmi, Vishal Sethi, Panagiotis Laskaridis, Andrew Rolt, and Pedro Cobas. Performance characteristics and optimisation of a geared intercooled reversed flow core engine. *Proceedings of the Institution of Mechanical Engineers, Part G: Journal of Aerospace Engineering*, 229(2):269–279, 2015.

[45] H. Grieb. *Projektierung von Turboflugtriebwerken*. Birkhäuser, ISBN 3-7643-6023-2, 2004.

[46] Edward MJ Naylor, Cecilia Ortiz Dueñas, Robert J Miller, and Howard P Hodson. Optimization of nonaxisymmetric endwalls in compressor s-shaped ducts. *Journal of Turbomachinery*, 132(1):011011, 2010.

[47] Abhijit Guha. Optimum fan pressure ratio for bypass engines with separate or mixed exhaust streams. *Journal of Propulsion and Power*, 17(5):1117–1122, 2001.

[48] Tadeusz Jozef Kotas. *The exergy method of thermal plant analysis*. Elsevier, 2013.

[49] JM Clarke and JH Horlock. Availability and propulsion. *Journal of Mechanical Engineering Science*, 17(4):223–232, 1975.

[50] María Vera-Morales and Cesare Hall. Modeling performance and emissions from aircraft in the aviation integrated modelling project. *Journal of Aircraft*, 47(3):812–819, 2010.

[51] CC Gleason and DW Bahr. Experimental clean combustor program, phase iii final report. *NASA CR-135384*, 1979.

[52] James H Bell and Rabindra D Mehta. Contraction design for small low-speed wind tunnels. 1988.

[53] Erwin Hartono, Maxim Golubev, Pirooz Moradnia, Valery Chernoray, and Håkan Nilsson. Piv measurement of air flow in a hydro power generator model. In *16th Int Symp on Applications of Laser Techniques to Fluid Mechanics*, 2012.

Part II
Appended Papers A–E

Paper A

Zhao, X., Grönstedt, T. and Kyprianidis, K., **Assessment of The Performance Potential for a Two-pass Cross Flow Intercooler for Aero Engine Applications**. The 21st ISABE conference, September 9-13, 2013, Busan, South Korea.

Paper B

Zhao, X. and Grönstedt, T., **Conceptual Design of a Two-Pass Cross Flow Aero-Engine Intercooler**. Proc IMechE Part G: Journal of Aerospace Engineering. 2014.

Paper C

Zhao, X., Thulin, O., and Grönstedt, T., **First and Second Law Analysis of Intercooled Turbofan Engine**. ASME Journal of Engineering for Gas Turbines and Power. 2015.

Paper D

Zhao, X. and Grönstedt, T., **Aero Engine Intercooling Optimization Using A Variable Flow Path**. The 22nd ISABE conference, October 25-30, 2015, Phoenix, USA.

Paper E

Zhao, X. Tokarev, M, Hartono, A E., Chernoray, V., and Grönstedt, T., **Experimental Validation of The Aerodynamic Performance of An Aero Engine Intercooler**. Submitted for publication in a scientific journal.